
COUPLED SEASONAL DATA ASSIMILATION OF SEA ICE, OCEAN, AND ATMOSPHERIC DYNAMICS OVER THE LAST MILLENNIUM

✉ Zilu Meng^{*1}, ✉ Gregory J. Hakim¹, and ✉ Eric J. Steig^{2,1}

¹ Department of Atmospheric and Climate Science, University of Washington, Seattle, WA

² Department of Earth and Space Sciences, University of Washington, Seattle, WA

January 27, 2025

ABSTRACT

“Online” data assimilation (DA) is used to generate a new seasonal-resolution reanalysis dataset over the last millennium by combining forecasts from an ocean–atmosphere–sea-ice coupled linear inverse model with climate proxy records. Instrumental verification reveals that this reconstruction achieves the highest correlation skill, while using fewer proxies, in surface temperature reconstructions compared to other paleo-DA products, particularly during boreal winter when proxy data are scarce. Reconstructed ocean and sea-ice variables also have high correlation with instrumental and satellite datasets. Verification against independent proxy records shows that reconstruction skill is robust throughout the last millennium. Analysis of the results reveals that the method effectively captures the seasonal evolution and amplitude of El Niño events. Reconstructed seasonal temperature variations are consistent with trends in orbital forcing over the last millennium.

SIGNIFICANCE STATEMENT

This paper introduces the first seasonal-resolution reanalysis of the last millennium, based on an “online” data assimilation method using a linear inverse model to assimilate paleoclimate proxies. We find good agreement when verifying the reconstruction against modern instrumental reanalyses and out-of-sample proxies. Results show that seasonal temperature trends are similar to predictions from orbital-insolation trends, and seasonal variability of modern El Niño events is similar to instrumental reanalyses.

1 Introduction

Reconstructions of past climate are essential for understanding the dynamics of the long-term climate system. Such reconstructions are particularly important in the context of global warming (Pachauri et al., 2007), as they place contemporary climate variability within a larger sample of past climate. This historical and long-term perspective also enhances our ability to improve projections of future climate change by providing a reference against which model simulations can be compared. Before the instrumental era, when humans began using scientific tools to record weather and climate information like temperature and precipitation, climate information is primarily derived from natural proxies such as tree rings, corals, and ice cores. For example, the width of some tree rings reflects local moisture and temperature stress (e.g., Briffa et al., 2004). This information can be used to reconstruct past climate conditions. The main challenges of using proxies to reconstruct past climate derive from their uneven spatial, temporal, and time-resolution, complicating multiproxy interpretations of climate variability. Recently, data-assimilation (DA) methods (e.g., Bouttier and Courtier, 2002) have been increasingly used to reconstruct past climates (e.g. Dirren and Hakim, 2005; Goosse et al., 2010; Widmann et al., 2010; Franke et al., 2017; Perkins and Hakim, 2021; Tardif et al., 2019; Steiger et al., 2018; Valler et al., 2024). This approach combines climate model physical constraints with proxy data to reconstruct climate variables. One of the most significant advantages of DA is that it allows for the reconstruction of variables not directly represented by the proxies (Hakim et al., 2016). For example, we can use temperature data from proxies to infer sea-ice conditions

*Correspondence author: Zilu Meng, zilumeng@uw.edu

and geopotential height, as there are strong and well-understood correlations among these variables (e.g. Hakim et al., 2016; Steiger et al., 2018; Brennan, 2022; Brennan and Hakim, 2022; Meng and Hakim, 2024).

A general and flexible paleoclimate data assimilation (PDA) framework, the Last Millennium Reanalysis (LMR), was proposed by Hakim et al. (2016) for reconstructing climate variables over the Common Era. The success of this framework has been followed by extensive research on PDA (e.g., Steiger et al., 2017; Dee et al., 2020; Sun et al., 2022; Luo et al., 2022; Meng and Hakim, 2024; Zhu et al., 2023; Okazaki et al., 2021; Hu et al., 2024). One practical limitation of PDA compared to weather DA is the high cost of forecasts that generate the prior (“first guess”), because of the need for long integrations of climate models (e.g., Taylor et al., 2012). Consequently, the initial LMR framework used an “offline” data assimilation (DA) method, where the prior is sampled from a static source, such as existing climate model simulations. This approach is effective when the predictive skill of climate fields is low relative to the computational expense (Okazaki et al., 2021).

There are, however, patterns of variability, such as the Pacific Decadal Oscillation (PDO) (Mantua and Hare, 2002) and El Niño South Oscillation (ENSO) (McPhaden et al., 2006; Meng and Li, 2024), that persist on seasonal to interannual timescales. Developing “online” PDA methods that exploit this persistence can lead to more accurate reconstructions, since the memory of past proxies is transmitted into the future by the forecast model. Using DA with a skillful coupled atmosphere–ocean model, information from terrestrial proxies such as tree-ring widths can be used to inform ocean state estimates, which then carry memory through ocean persistence. An example of this online PDA approach is shown by Perkins and Hakim (2021), who used a linear inverse model (LIM) to reconstruct climate fields over the last millennium and found improved representations of decadal variability.

A significant challenge with PDA reconstructions is resolving the seasonal cycle. For example, proxies from Northern Hemisphere trees, including tree-ring width (TRW) and latewood density, primarily reflect warm-season temperature (PAGES2k Consortium, 2013; PAGES2k Consortium and others, 2017). Previous PDA studies have used this information to reconstruct annual-mean climate variability, leading to biases in the reconstructions and inconsistent results for significant climate periods such as the Medieval Climate Anomaly and the Little Ice Age (PAGES2k Consortium and others, 2017; Hakim et al., 2016; Tardif et al., 2019; Steiger et al., 2018). Here, we present results for a seasonal reconstruction of the last millennium using online PDA. We use a LIM to forecast one season to the next: from March-May (MAM) to June-August (JJA), from JJA to September-November (SON), from SON to December-February (DJF), and from DJF to the next year.

The LIM incorporates sea-ice variables (concentration and thickness), recognizing the long-lead memory of sea ice (Blanchard-Wrigglesworth et al., 2011) and therefore predictive skill, especially near the Arctic where seasonal variability is large. We assimilate proxies from the PAGES2k V2 (PAGES2k Consortium and others, 2017) database at the season specific to each proxy. Proxies that represent annual-mean conditions are assimilated subsequently once an annual mean forecast is available from the initial LIM forecast from seasonal proxies only.

The organization of the remainder of the paper is as follows. Section 2 details the PDA methods and data used in this study, and Section 3 presents instrumental and proxy verification to measure the accuracy of the reconstruction. Section 4 applies the reconstruction to analyze seasonal climate variability and trends over the last millennium. Section 5 provides a concluding discussion.

2 LMR-Seasonal Framework Data and Methods

The LMR-Seasonal approach utilizes an online “cycling” DA framework, consisting of three components. First, a LIM is trained for seasonal forecasting as described in Subsection 2.1. Second, proxy system models, which estimate the proxies from the prior, are trained as described in Subsection 2.2. Third, an Ensemble Kalman Filter (EnKF) is used to combine the proxy and prior as described in Subsection 2.3.

2.1 Linear Inverse Model (LIM)

Linear Inverse Models are a computationally efficient, widely applied, and skillful method for predicting climate fields (e.g. Penland and Magorian, 1993; Penland, Cécile and Sardeshmukh, Prashant D, 1995; Newman, 2013; Perkins and Hakim, 2020; Meng and Hakim, 2024). A LIM captures linear dynamics of anomalies about a mean state:

$$\frac{d\mathbf{x}}{dt} = \mathbf{L}\mathbf{x} + \boldsymbol{\xi}, \quad (1)$$

where \mathbf{x} is the state vector. \mathbf{L} is a matrix representing deterministic dynamics, and $\boldsymbol{\xi}$ is a random noise vector, which is temporally uncorrelated, but may have correlations in the state space \mathbf{x} . For a stable linear system, the eigenvalues of \mathbf{L} are negative (Penland and Magorian, 1993).

In this study, \mathbf{x} represents low-dimensional principal components (PCs) derived from a truncated set of empirical orthogonal functions (EOFs). EOF truncation is applied to individual variables of interest, including 2-meter temperature (TAS), sea surface temperature (TOS), ocean heat content from 300 meters to the surface (OHC300), Northern Hemisphere (NH) sea-ice thickness (SIT), and NH sea-ice concentration (SIC). We do not include Southern Hemisphere (SH) sea-ice due to the sparseness of SH paleoclimate proxies, and known challenges in reconciling climate model simulations of SH sea-ice with observations (Roach et al., 2020). This selection of variables is guided by two primary considerations: (1) we limit the number of PCs within the LIM to prevent over-fitting, which could degrade the quality of reconstructions; (2) we exclude high-frequency atmospheric variables such as sea-level pressure (SLP) to avoid reducing the forecast skill of the primary variables of interest. For all variables except OHC300, we select the first 15 PCs, which account for around 80% of the total variance of each variable. Following Perkins and Hakim (2020), we select 30 PCs for OHC300 to better capture the extended memory of this variable within the LIM. Thus, the state vector is defined as:

$$\mathbf{x} = [\mathbf{PC}_{\text{TAS}}^T, \mathbf{PC}_{\text{TOS}}^T, \mathbf{PC}_{\text{OHC300}}^T, \mathbf{PC}_{\text{SIT}}^T, \mathbf{PC}_{\text{SIC}}^T]^T. \quad (2)$$

Linear Inverse Model training process. We utilize output from two models in the Coupled Model Intercomparison Project Phase 5 (CMIP5) Last Millennium experiments, specifically CCSM4 and MPI-ESM-R (Taylor et al., 2012). We choose these models primarily to maintain consistency with LMR v1 (Hakim et al., 2016), LMR v2 (Tardif et al., 2019), and LMR online (Perkins and Hakim, 2021). Furthermore, seasonal climate variability statistics have not changed significantly from CMIP5 to CMIP6 (Brown et al., 2020). We define four seasons by three-month averages: March-April-May (MAM), June-July-August (JJA), September-October-November (SON) and December-January-February (DJF). Prior to taking the seasonal average, model output data are placed on a 2×2 latitude-longitude grid using linear interpolation in the Climate Data Operators package (Schulzweida et al., 2019), and the last millennium trend for each month is removed by simple linear regression. EOF analysis on area-weighted variables yields the first 15 PCs for each variable (30 PCs for OHC300). Then, \mathbf{L} is calculated by

$$\mathbf{L} = \tau^{-1} \ln \mathbf{C}(\tau) \mathbf{C}(0)^{-1}. \quad (3)$$

Here $\mathbf{C}(\tau)$ is the τ -lag covariance matrix of \mathbf{x} , $\mathbf{C}(\tau) = \langle \mathbf{x}(\tau) \mathbf{x}^T(0) \rangle$, where “ $\langle \rangle$ ” represents a sample average. Here τ is 3 months for our seasonal LIM. The stochastic part of the dynamics, ξ , has covariance matrix \mathbf{Q} , such that $\langle \xi \xi^T \rangle = \mathbf{Q}$. \mathbf{Q} is calculated based on stationary statistics:

$$\frac{d\mathbf{C}(0)}{dt} = \mathbf{L}\mathbf{C}(0) + \mathbf{C}(0)\mathbf{L}^T + \mathbf{Q} = 0. \quad (4)$$

Using \mathbf{Q} and \mathbf{L} , stochastic integration of (1) yields a sample trajectory using the two-step integration process of Penland and Matrosova (1994):

$$\mathbf{x}_{t+\delta t} = (\mathbf{L}\delta t + \mathbf{I})\mathbf{x}_t + \hat{\mathbf{Q}}\sqrt{\Lambda\delta t}\boldsymbol{\alpha} \quad (5)$$

$$\mathbf{x}_{t+\delta t/2} = \frac{1}{2}(\mathbf{x}_{t+\delta t} + \mathbf{x}_t), \quad (6)$$

where δt is the integration time step, set at 6 hours for this study. \mathbf{I} is the identity matrix, $\hat{\mathbf{Q}}$ denotes the matrix where columns are eigenvectors of \mathbf{Q} and Λ is the diagonal matrix of eigenvalues of \mathbf{Q} . $\boldsymbol{\alpha}$ is a vector of independent standard normal random variables. We exclude eigenvectors associated with negative eigenvalues in \mathbf{Q} and normalize the remaining eigenvalues to preserve total variance, following Penland and Matrosova (1994) and Perkins and Hakim (2020). After training the LIM on output from CCSM4 and MPI-ESM-R last millennium simulations (850 C.E.–1850 C.E.) (Taylor et al., 2012), the LIM demonstrates predictive skill to at least 12 months as evidenced by out-of-sample tests shown in Supplementary Fig. S1 and S2.

2.2 Proxy System Models

We use the temperature-sensitive PAGES2k V2 dataset (PAGES2k Consortium and others, 2017) as the observational inputs for our data assimilation process. The PAGES2k V2 dataset comprises approximately 700 proxy records, mainly from tree rings, corals and ice cores. We calibrate PSMs for each proxy record, using surface temperatures from GISTEMP v4 (Lenssen et al., 2019) for terrestrial proxies and Sea Surface Temperature (SST) from ERSST v5 (Huang et al., 2017) for marine records. Comparisons with calibration on other instrumental observations, such as Berkeley Earth (Rohde and Hausfather, 2020) and MLOST (Smith et al., 2008), yield similar results (not shown).

The truncated EOF basis of the LIM does not fully resolve local details of climate fields such as surface temperature and SST, which is a “representativeness” error we account for by calibrating the PSMs in the EOF-truncated space,

$\hat{\mathbf{x}} = \mathbf{U}\mathbf{U}^T\mathbf{x}$, where \mathbf{U}^T is the matrix with the first 15 PCs derived from EOF analysis:

$$\mathbf{y} = \mathbf{H}\hat{\mathbf{x}} + \epsilon. \quad (7)$$

Here, \mathbf{H} is the matrix that maps the climate variables to the proxy data, \mathbf{y} , and ϵ is the error term.

As will be discussed in section 2.3, an important factor for data assimilation is the observation error covariance matrix $\mathbf{R} = \langle \epsilon\epsilon^T \rangle$. [Hakim et al. \(2022\)](#) employ linear regression to estimate \mathbf{H} and a full covariance matrix \mathbf{R} . In our study, we adopt a similar method but with a diagonal \mathbf{R} , implying zero error covariance among errors for the proxy PSMs. The use of a full \mathbf{R} matrix is impractical because the calibration period does not provide sufficiently long overlap between each of the proxies to estimate the off-diagonal terms, and tests suggest that the diagonal values of \mathbf{R} are several orders of magnitude larger than the off-diagonal elements (not shown).

Seasonality. Seasonality refers to the specific season that a proxy’s temperature represents. [Tardif et al. \(2019\)](#) assessed both expert-based seasonality, derived from PAGES2k metadata, and objectively-determined seasonality, given by the best correlation with instrumental data during PSM calibration. We evaluate both definitions of seasonality and find no significant differences in calibration results (compare Fig. 1 with Supplementary Fig. S3), or in the PDA results as measured by instrumental verification (compare Fig. 3 with Supplementary Fig. S4; and Fig. 4 with Supplementary Fig. S5) and independent proxies (compare Fig. 11 with Supplementary Fig. S8; see Section 3). We therefore use the objectively-determined seasonality to maintain consistency with LMR v2 ([Tardif et al., 2019](#)) and LMR Online ([Perkins and Hakim, 2021](#)). We note that sub-seasonal coral records are averaged to seasonal resolution (DJF, MAM, JJA, SON) for PSM calibration and assimilation.

We remove proxies from assimilation if they have an insignificant correlation with local temperature or high temporal error autocorrelation. Specifically, we remove proxies that have a PSM calibration correlation below 0.05, or a one-year lag auto-correlation in PSM calibration residuals exceeding 0.90. As shown in Fig. 1, some Pacific corals have high PSM calibration correlation but also a high 1-year-lag error auto-correlation. High error autocorrelation is problematic for Kalman filters, which assume that observation errors are uncorrelated in time.

2.3 Ensemble Kalman Filter and Update Strategy

Here we introduce the update strategy for our seasonal reconstruction.

Ensemble Kalman Filter. DA in this study is conducted using an EnKF as described by [Evensen \(2003\)](#). The EnKF is extensively applied in a variety of paleo-DA tasks and has consistently shown strong performance ([Hakim et al., 2016](#); [Franke et al., 2017](#); [Perkins and Hakim, 2021](#); [Steiger et al., 2018](#); [Zhu et al., 2022](#); [Valler et al., 2024](#)). The primary step in the EnKF process is the “update”,

$$\mathbf{x}_a = \mathbf{x}_p + \mathbf{K}[\mathbf{y} - \mathcal{H}(\mathbf{x}_p)], \quad (8)$$

where \mathbf{x}_a represents the posterior (“analysis”) state vector, \mathbf{x}_p denotes the prior state vector and \mathcal{H} is the observation operator that maps to the corresponding observation vector (i.e., the PSMs). Matrix \mathbf{K} , the Kalman Gain, is defined by,

$$\mathbf{K} = \mathbf{B}\mathbf{H}^T [\mathbf{H}\mathbf{B}\mathbf{H}^T + \mathbf{R}]^{-1}, \quad (9)$$

where \mathbf{B} is the prior covariance matrix and \mathbf{H} is the linearization of \mathcal{H} . \mathbf{R} is the observation error covariance matrix derived from Equation 7. Given that all PSMs in this study are linear, $\mathcal{H} = \mathbf{H}$. To solve 8 and 9 using ensemble sampling, we employ the Ensemble Square Root Filter (EnSRF) method ([Whitaker and Hamill, 2002](#)) incorporating a serial observation update strategy. For the k th proxy, whose value is y_k , the update proceeds by separating the ensemble into ensemble mean ($\bar{\mathbf{x}}$) and perturbations (\mathbf{x}'_i):

$$\mathbf{x} = \bar{\mathbf{x}} + \mathbf{x}'_i. \quad (10)$$

For the ensemble mean $\bar{\mathbf{x}}$, the update equation is

$$\bar{\mathbf{x}}_a = \bar{\mathbf{x}}_p + \frac{\text{cov}(\mathbf{x}_p, y_{e,k})}{\text{var}(y_{e,k}) + R_k} (y_k - \bar{y}_{e,k}), \quad (11)$$

where $y_{e,k}$ denotes the k th proxy estimate from from the ensemble, represented as $y_{e,k} = \bar{y}_{e,k} + y'_{e,k}$, and R_k is the k th proxy error variance. The “var” and “cov” operators denote the variance and covariance, respectively. Ensemble

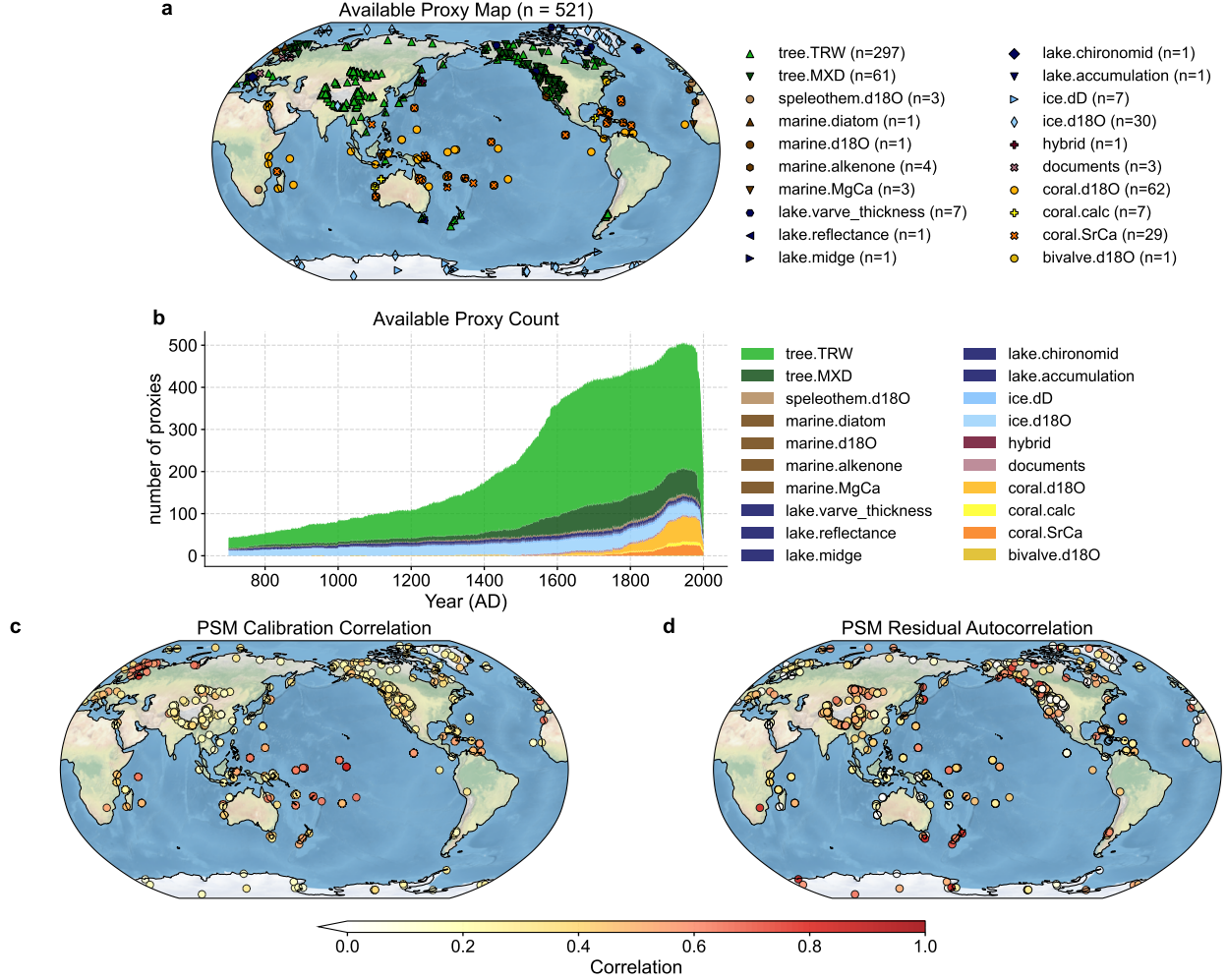


Figure 1: **Proxies from PAGES2k V2 (PAGES2k Consortium and others, 2017)**. **a**. Locations and counts of proxy types after filtering by the specified standards indicated by the Subsection 2.2. **b**. Evolution of the number of proxies over time. **c–d**. Spatial distribution of PSM calibration correlations and 1-year lag residual (error) auto-correlations.

perturbations \mathbf{x}'_i , are update by

$$\mathbf{x}'_a = \mathbf{x}'_p - \left[1 + \sqrt{\frac{R_k}{\text{var}(y_{e,k}) + R_k}} \right]^{-1} \frac{\text{cov}(\mathbf{x}_p, y_{e,k})}{\text{var}(y_{e,k}) + R_k} (y'_{e,k}). \quad (12)$$

This ensemble update is completed for the i -th member using (10) to obtain the full analysis state. In this study, the ensemble size is 800, which allows us to avoid ensemble inflation and localization methods (e.g., Anderson, 2012). Localization techniques are complicated by the EOF state space of the LIM, so we use an ensemble large enough to minimize the need for such localization.

Seasonal Update Strategy Unlike previous PDA reconstructions (e.g. Hakim et al., 2016; Steiger et al., 2018; Tardif et al., 2019; Perkins and Hakim, 2021) that use seasonal proxies to update the annual mean, our approach updates specific seasons corresponding to the proxy seasonality. An example illustration of this update strategy is shown in Fig. 2 for three proxies having different seasonality: DJF, MAMJJA and DJFMAMJJASON. When the LIM forecast completes the DJF season, the DJF proxy is used to update the DJF prior ensemble. Subsequently, the LIM advances by updating the state to the MAM and JJA seasons. Upon reaching JJA, the MAMJJA proxy is used to update MAM and JJA ensembles. Finally, when the LIM ensemble progresses to the SON season, the DJFMAMJJASON proxy is used to update the DJF, MAM, JJA and SON ensembles. In summary, our methodology emphasizes a season-to-season

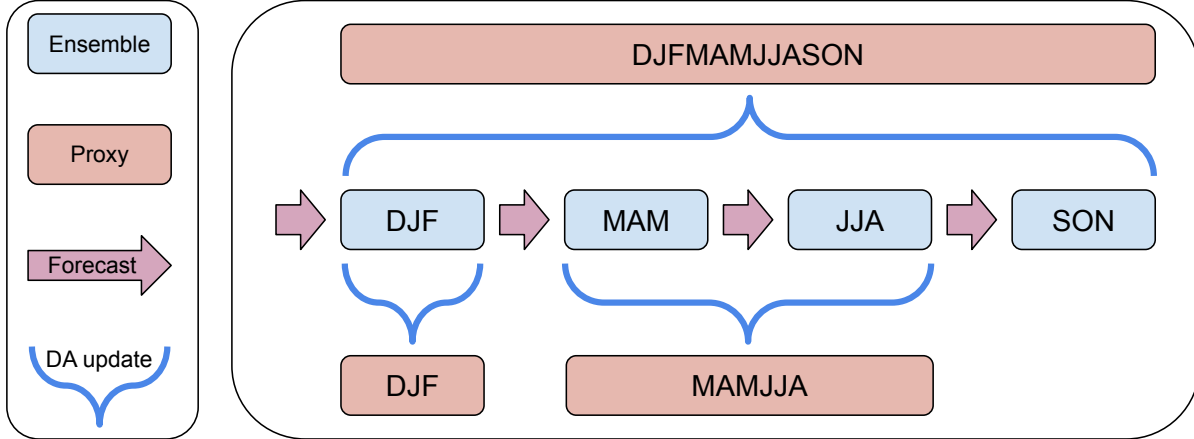


Figure 2: **LMR Seasonal update strategy.** The light blue box represents the ensemble, the rose box the proxy, and the pink arrow the forecast step from the LIM. Curly brackets denote the update from the EnKF to integrate the proxy data into updating the prior ensemble. The text within the box indicates the seasonality of either the ensemble or the proxies.

update mechanism. This novel update strategy has a significant impact on reconstructions of the differences between the Medieval Climate Anomaly (MCA) and Little Ice Age (LIA), as discussed in Section 4.

2.4 Verification Metrics

We validate the LMR Seasonal reconstruction against both calibration and reanalysis datasets (discussed below) using two primary verification metrics: correlation,

$$\text{corr} = \frac{1}{n} \sum_{i=1}^n \frac{(x_i - \bar{x})(v_i - \bar{v})}{\sigma_x \sigma_v}, \quad (13)$$

and the coefficient of efficiency (CE) (Nash and Sutcliffe, 1970),

$$\text{CE} = 1 - \frac{\sum_{i=1}^n (v_i - x_i)^2}{\sum_{i=1}^n (v_i - \bar{v})^2}. \quad (14)$$

Here an overbar (\bar{x}) represents a mean value, σ represents the standard deviation, and x and v represent the reconstructed and verification values, respectively. Correlation measures errors in signal timing, whereas CE measures errors in signal timing and amplitude.

2.5 Comparisons to other PDA Last Millennium Reconstructions

To assess agreement with other PDA products, we compare our results to three DA products over the last millennium: PHYDA (Steiger et al., 2018), LMR v2 (Tardif et al., 2019) and LMR online (Perkins and Hakim, 2021). Details on the DA methods, proxy number and time resolution for each product are given in Table 1. Besides LMR-Seasonal, only PHYDA provides reconstructions for DJF and JJA (but not for SON or MAM), while LMR v2 and LMR Online are limited to annual means. A significant distinction between the “online” and “offline” DA methods involves whether the prior is derived from random (time-independent) draws from an existing climate model simulation (offline) or from a forecast of the analysis at the previous assimilation time (online). An advantage of the online DA method is that the “memory” of past proxy information is carried to the next assimilation time. This feature is particularly vital for our seasonal DA approach, as NH trees are the dominant source of the climate signal, and are primarily sensitive to summer growing conditions. With “online” DA, the JJA posterior, for example, serves as the initial condition for the SON prior, informing the SON and future season’s reconstructions. This results in more information persisting into seasons with fewer proxies (e.g., Winter and Spring).

Table 1: Summary of Data Assimilation Products over the Last Millennium

Name	PDA Method	N_{proxy}^1	Time Resolution	Reference
PHYDA	Offline	2978	(Sub)Annual ²	Steiger et al. (2018)
LMR v2	Offline	2250	Annual	Tardif et al. (2019)
LMR Online	Online	545	Annual	Perkins and Hakim (2021)
LMR Seasonal	Online	521	Seasonal ³	this study

¹ N_{proxy} denotes the total number of proxies for data assimilation.

² “(Sub)Annual” refers to PHYDA’s time resolutions finer than a year, because it has the annual mean, DJF and JJA reconstructions, and monthly Niño 3.4 Index reconstructions.

³ “Seasonal” refers to 4 time steps (MAM, JJA, SON, DJF) every year.

3 Verification

We verify our reconstruction using instrumental observations and proxy data, as described below. For instrumental verification, we use 2m air temperature from HadCRUT5 (Morice et al., 2021) and the ERA-20C Reanalysis (Poli et al., 2016), ocean temperature data from Hadley EN4 (Good et al., 2013), SST from HadISST (Rayner et al., 2003) and sea-ice concentration from the satellite dataset of Fetterer et al. (2017). For proxy data verification we use the PAGES2k V2 dataset (PAGES2k Consortium and others, 2017) by withholding some proxies from assimilation using the bootstrap procedure described below.

3.1 Instrumental Verification

Measured by correlation with the HadCRUT5 instrumental dataset during 1880–2000 CE, the LMR Seasonal reconstruction skill in annual-mean 2m air temperature is similar to or better than other reconstructions in the global mean (Fig. 3) despite assimilating fewer proxies. The spatial correlation pattern shows that LMR Seasonal performs better than LMR v2 primarily in Europe, the North Pacific Ocean, the Indian Ocean, and the South Atlantic Ocean, but less well over the Southern Ocean and portions of Asia. Compared to PHYDA, the most pronounced differences are found in the Southern Ocean and the Indian Ocean. Similar results are found when verifying against the ERA-20C Reanalysis (Supplementary Fig. S6 and S7). The limited number of proxies in the Southern Hemisphere means that the main signal for reconstructing the Southern Ocean relies heavily on long-distance teleconnections in the model prior. Since we do not use covariance localization, it is possible that bias in the Southern Ocean teleconnections from LIM forecasts degrade the performance of LMR Seasonal in this location. We note that in Antarctica, where there are abundant ice core records (e.g., Steig et al., 2013; Stenni et al., 2017), the reconstructions perform comparatively well, with LMR Seasonal generally being superior.

Seasonal verification against HadCRUT5 reveals that LMR Seasonal has skill globally with positive correlations almost everywhere (Fig. 4). Compared to PHYDA, which is the only other reconstruction that includes DJF and JJA reconstructions, LMR Seasonal performs relatively better during DJF than JJA, which we attribute to the sparse proxy data during DJF compared to JJA. PHYDA performs better during Northern Hemisphere summer, particularly over North America and Eurasia, which we attribute to the much large number of tree-ring proxies that PHYDA assimilates in these locations.

We verify upper-300m ocean-heat content (OHC300) against the Hadley EN4 dataset (Good et al., 2013) (Fig. 5) and Arctic sea-ice concentration (SIC) against the satellite observations Fetterer et al. (2017) (Fig. 6). Despite not incorporating any direct observations of these quantities, the LMR Seasonal reconstruction show high correlation with the verification datasets. For OHC300, skill is highest in the tropical Pacific, the eastern North Pacific, and northern Atlantic Ocean regions. Skill in SIC is highest in Hudson Bay, and near sea-ice edges, especially around Greenland and the Barents Sea. Skill is lowest in the Beaufort Sea during DJF and MAM, seasons where proxies are least abundant. In contrast, SIC generally exhibits higher correlations in JJA compared to other seasons. We speculate that this is due to SIC having a stronger correlation with 2m air temperature in JJA compared to other seasons (Blanchard-Wrigglesworth et al., 2011).

Comparing the LMR Seasonal global mean temperature (GMT) and Niño3.4 Index with values from the instrumental datasets HadCRUT5 and HadISST shows highly skillful reconstructions (Figs. 7 and 8). Specifically, GMT has a correlation with HadCRUT5 of about 0.9 in all seasons and in the annual mean. The Niño3.4 Index, which represents the intensity of ENSO, shows a correlation (CE) around 0.8 (0.55) in all seasons. The use of seasonal coral data significantly improves the accuracy of the reconstruction compared to annualized coral data, which shows a correlation (CE) of

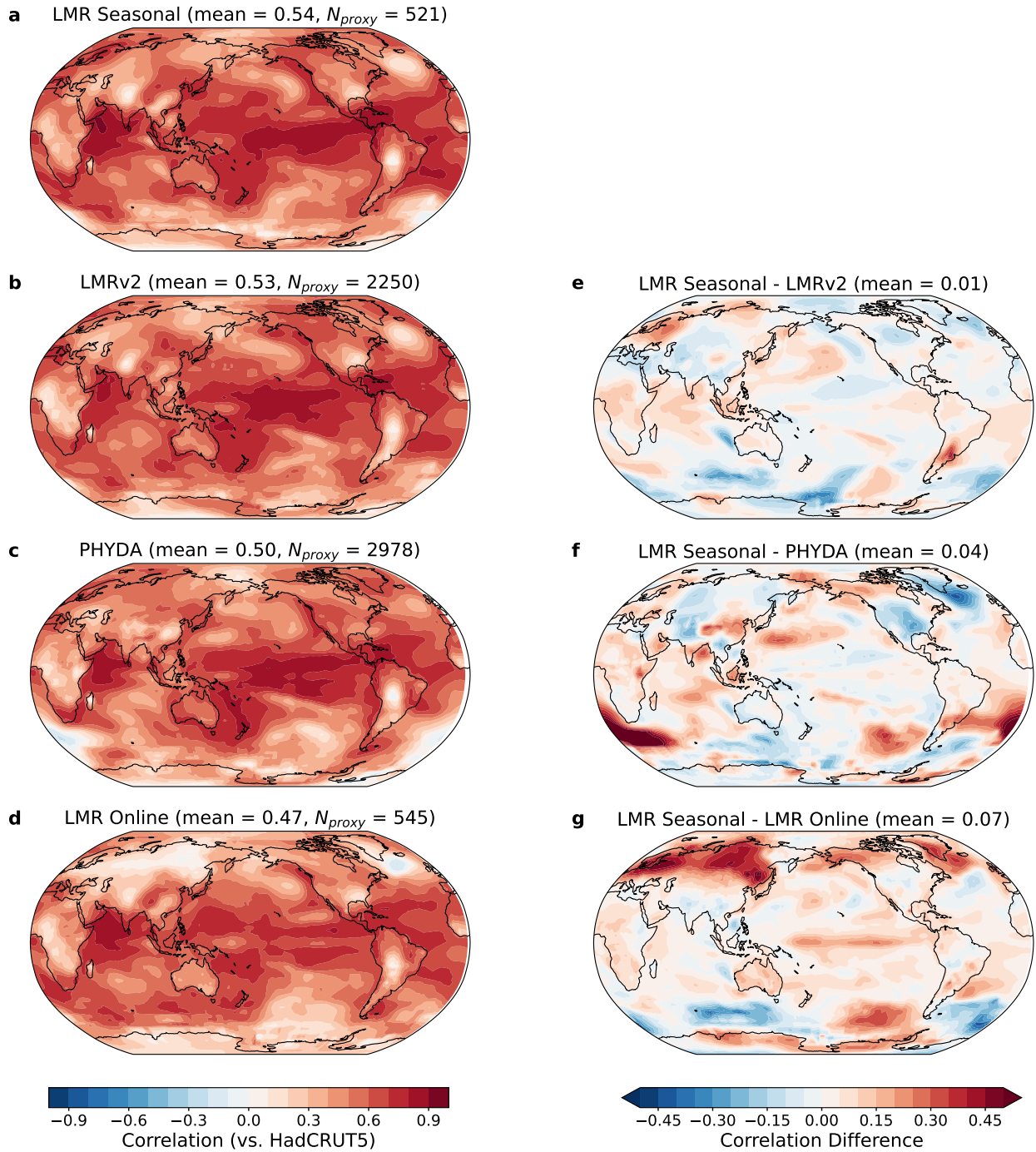


Figure 3: Annual mean surface temperature instrumental verification. a–d. Correlation between various DA reconstructions and HadCRUT5 (Morice et al., 2021) 2m air temperature during 1880–2000. Results are shown for (a) LMR Seasonal, (b) LMRv2, (c) PHYDA, (d) LMR Online) with the global-mean correlation and the number of used proxies given in the title for each subpanel. Correlation difference between LMR Seasonal (a) and other reconstructions are shown for (e) LMRv2, (f) PHYDA, (g) LMR Online), with global-mean correlation differences indicated in the titles.

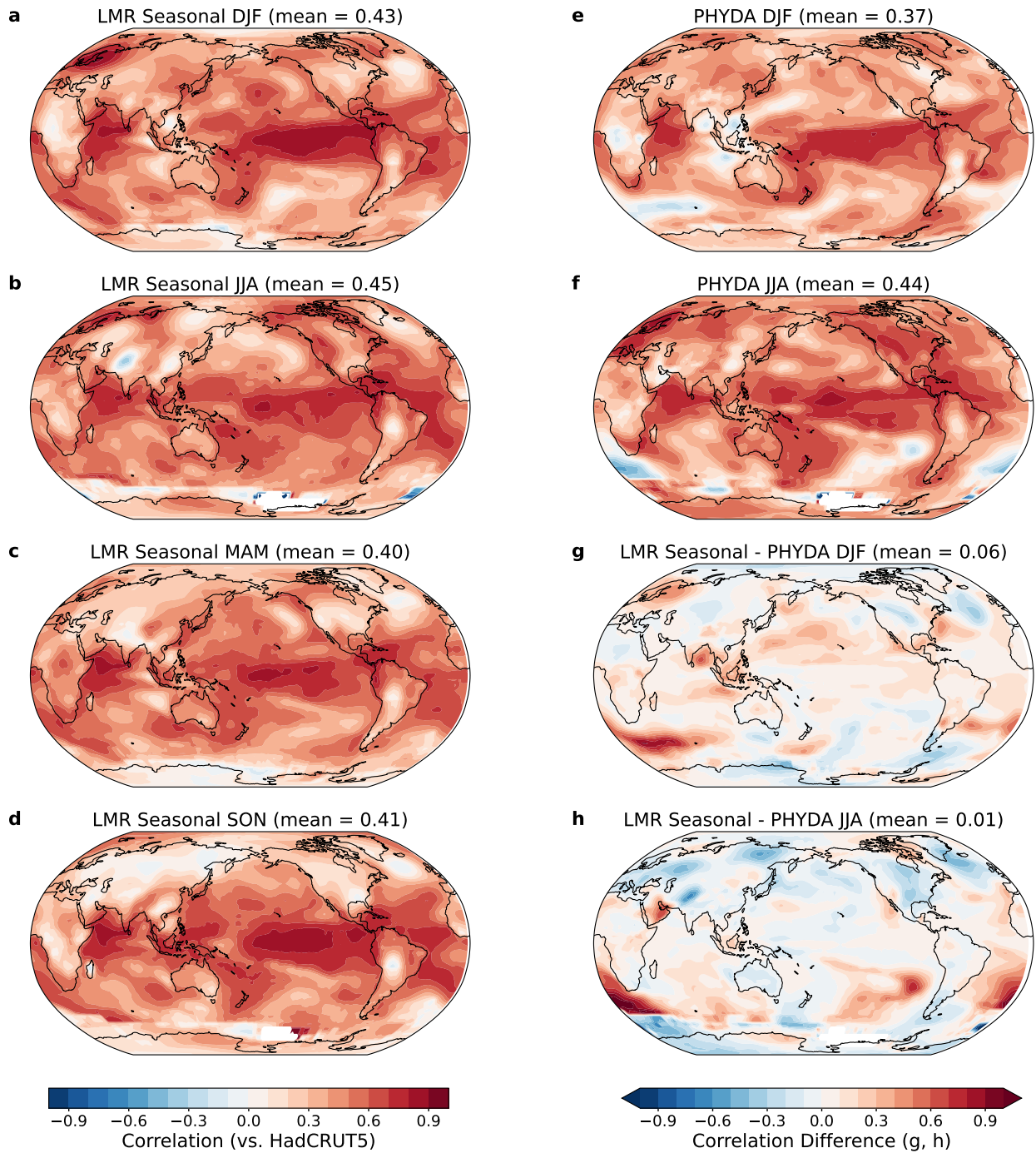


Figure 4: **Surface temperature seasonal instrumental verification a–d.** The correlations between the LMR Seasonal and HadCRUT5 (Morice et al., 2021). For DJF (a), MAM (c), JJA (b), and SON (d) during 1880–2000. **e–f.** Correlations between PHYDA and HadCRUT5 are shown for DJF (e) and JJA (f). **g–h.** The correlation differences between LMR Seasonal and PHYDA in DJF (g) and JJA (h).

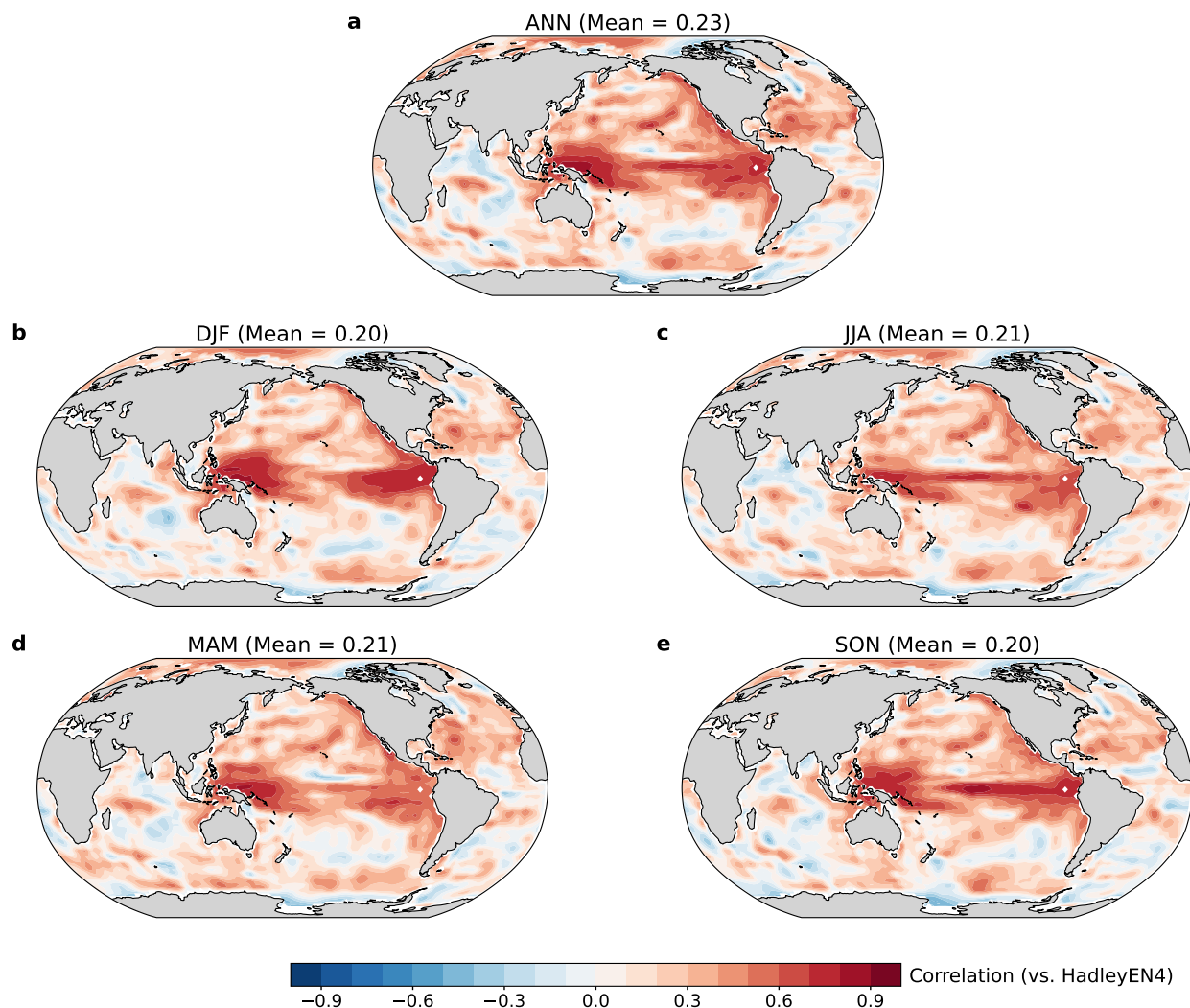


Figure 5: **Ocean heat content from 300m to the surface (OHC300) instrumental verification.** Correlation between LMR Seasonal OHC300 and HadleyEN4 OHC300 (Good et al., 2013) over the period 1940–2000 for the annual mean (a), DJF (b), JJA (c), MAM (d), and SON (e). Global-mean correlations are indicated in the titles.

approximately 0.7 (0.3) with the annual coral reconstructions and HadISST (not shown). In addition, compared to PHYDA, our reconstruction has higher correlation and CE in all seasons except in JJA’s correlation (Supplementary Fig. S8). The greatest contribution to improved ENSO reconstruction likely comes from the online DA scheme, since ENSO exhibits forecast skill on seasonal to annual timescales (McPhaden et al., 2006; Perkins and Hakim, 2020); information from the previous season persists to subsequent seasons, providing a more accurate prior.

The ENSO reconstruction allows us to investigate the variability of El Niño over the last millennium with a much larger sample than is available during the instrumental period. Following Wang et al. (2019), we categorize El Niño events into four classes based on their onset phase evolution: Strong Basin Wide (SBW), Moderate Eastern Pacific (MEP), Moderate Central Pacific (MCP), and Successive. The composite analysis of El Niño cases from 1900 to 2000 based on this classification is illustrated in Fig. 9. As described by Wang et al. (2019), SBW events are characterized by a combination of eastward SSTA from the western Pacific and westward SSTA from the eastern Pacific, leading to strong warming events (“super El Niño”). In contrast, MEP and MCP events are defined by westward and eastward SSTA from the eastern and western Pacific, respectively, resulting in moderate warming. Successive cases describe two consecutive years of sustained El Niño conditions. Compared to HadISST data, the LMR Seasonal reconstruction successfully captures most of the seasonal evolution of these four El Niño classes, although the amplitude of the SBW and MEP cases is smaller in the reconstruction than in HadISST. The most significant discrepancies occur for MCP due to the small sample size (3 events), since most cases are after the year 2000; many regions still align well

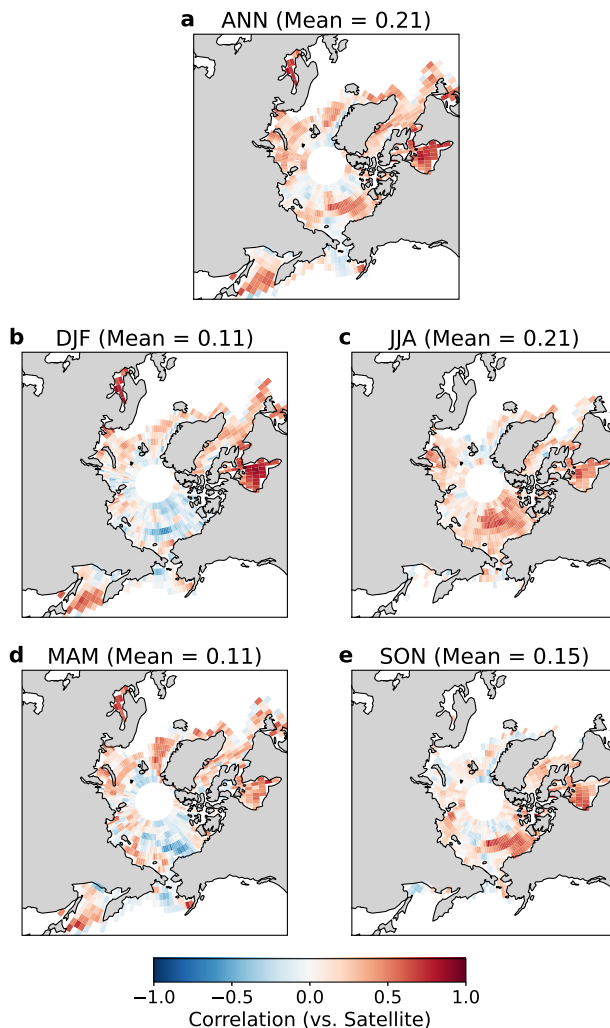


Figure 6: **Northern Hemisphere sea-ice concentration (SIC) instrumental verification.** Correlation between the LMR Seasonal SIC and satellite SIC data (Fetterer et al., 2017) during 1980–2000 are presented for the annual mean (a), DJF (b), JJA (c), MAM (d), and SON (e). Global-mean correlations are indicated in the titles.

with HadISST observations. Furthermore, as depicted in Fig. 10, all four SBW cases demonstrate consistent evolution with the reconstructed Niño3.4 index evolution, closely following the HadISST time series. In comparison, the PHYDA reconstruction does not align as closely with HadISST, especially during JJA and SON.

In summary, instrumental verification shows that the LMR Seasonal reconstruction faithfully captures a wide range of coupled atmosphere–ocean–sea-ice climate variability in space and time during the instrumental period.

3.2 Independent Proxy Verification

To assess the robustness of LMR Seasonal in the pre-instrumental period (800–1850 CE), we validate against proxies left out of the assimilation process following Hakim et al. (2016). We employ the bootstrap method, randomly omitting 20% of the proxies and conducting DA across 50 epochs. For each epoch, the proxies are forward modeled from the reconstructed climate states using the PSM (7) for each proxy, yielding a direct comparison of the LMR Seasonal reconstruction to both the assimilated and independent proxy chronologies. The comparison is summarized by the time series correlation between the reconstructed and actual proxy time series. For the assimilated proxies, we find that the distribution of correlation values during the calibration and pre-calibration periods is very similar, suggesting a robust PSM relationship (Fig. 11). Results for non-assimilated proxies are similar, but with somewhat lower correlation values. There are no significant differences between these results and those when seasonality is defined by the expert-based

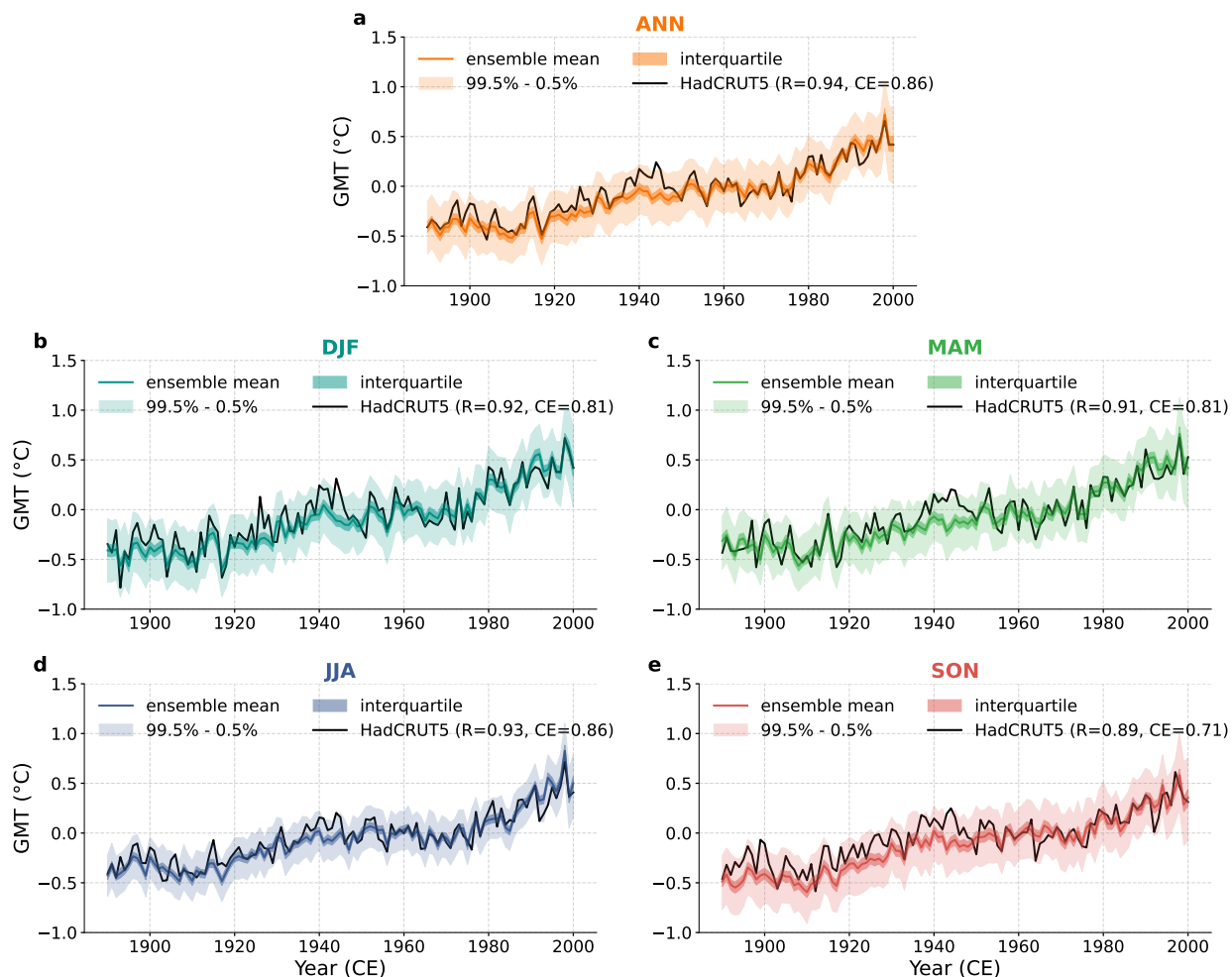


Figure 7: **Global mean surface temperature (GMT) instrumental verification.** Temporal verification of the ensemble-mean LMR Seasonal reconstructed GMT series (colored curves) against HadCRUT5 (Morice et al., 2021) GMT (black solid curve) in annual mean (a), DJF (b), MAM (c), JJA (d), and SON (e). The reference time period for anomalies is 1950–1980. For each reconstruction, dark shading denotes the ensemble interquartile range, and light shading the 0.5% to 99.5% interval. R = correlation, CE = coefficient of efficiency.

seasonality defined in the PAGES2K database results (cf. Fig. 11 and Supplementary Fig. S9). This indicates that the results are insensitive to the exact definition of proxy seasonality.

4 Last Millennium Seasonal Temperature Trends, Medieval Climate Anomaly and Little Ice Age

From 850–1850 CE, most proxy evidence suggests that Earth experienced a cooling climate trend driven by orbital forcing and significant volcanic eruptions (McGregor et al., 2015). We compare our reconstructed seasonal temperature trends with seasonal trends from the CCSM4 Last Millennium simulation, as depicted in Fig. 12 and Supplementary Fig. S10. Both the reconstructed and modeled trends show enhanced cooling in DJF and SON relative to MAM and JJA, which have smaller trends. This seasonal difference is attributed to the delayed climate response to orbital forcing (Fig. 12 b, red dashed curve), as discussed by Lücke et al. (2021). It is important to note that the LIM trained on this model simulation has no trend, and no season-specific variability (i.e., a single LIM is used for all seasons); the reconstructed seasonal trends arise solely from assimilation of proxy data.

Over the Last Millennium, two significant periods of multicentennial climate variability are the Medieval Climate Anomaly (MCA) and the Little Ice Age (LIA). Following Mann et al. (2009), we define the MCA as the period from

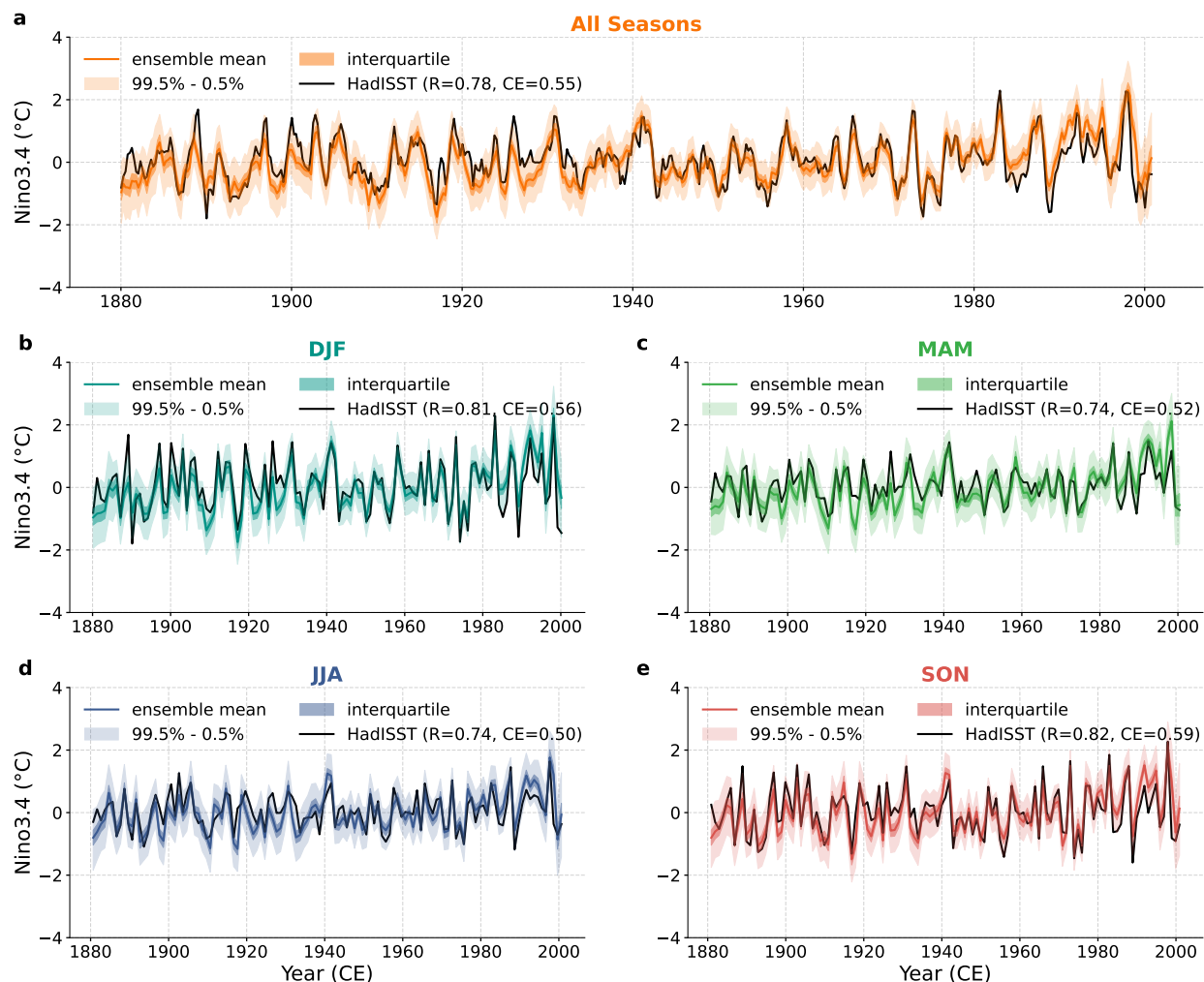


Figure 8: **Niño3.4 index instrumental verification.** Temporal verification of the ensemble mean LMR Seasonal reconstructed Niño3.4 Index (colored curves) against HadISST (Rayner et al., 2003) (black solid curve) in all seasons (a), DJF (b), MAM (c), JJA (d), and SON (e). Dark shading denotes the interquartile range, and light shading the 0.5% to 99.5% interval. R = correlation, CE = coefficient of efficiency.

950 CE to 1250 CE and the LIA from 1400 CE to 1700 CE. Comparing the annual-mean global-mean temperature in LMR Seasonal with three other reconstructions, we find that LMR Seasonal has larger multicentennial variability, especially with respect to the MCA-LIA difference (Fig. 13a). The spatial pattern of temperature differences between these two time periods (MCA-LIA) reveals a common pattern of Arctic-amplified warming among the reconstructions (Fig. 13b–e). Notable differences are the much larger amplitude signal in LMR Seasonal, and the opposite sign of tropical Pacific temperature difference when compared with PYHDA. Moreover, LMR Seasonal shows an MCA-LIA pattern over parts of Antarctica and the Southern Ocean that is mostly absent in the other reconstructions. This pattern is consistent with the independent temperature reconstruction of Orsi et al. (2012) based on a borehole thermometry analysis in West Antarctica (Supplementary Fig. S11). We attribute these high-latitude differences to polar amplification having larger amplitude on seasonal time scales, which leads to more signal in the annual mean (Supplementary Fig. S12).

As discussed above with regard to seasonal temperature trends, summer exhibits the least cooling trend over the last millennium, attributable to differences in insolation trends and seasonal lag due to ocean heat content (Lücke et al., 2021). Most proxies, especially NH tree ring width and latewood density, predominantly record JJA temperatures (e.g., Briffa et al., 1992; Anchukaitis et al., 2017). Annual-mean data assimilation dilutes the influence of JJA proxies, which likely reduces cooling trends over the Last Millennium. Our seasonal-update strategy ensures that connections between seasons are dynamically connected by the LIM, rather than static as in offline DA approaches. We hypothesize that these

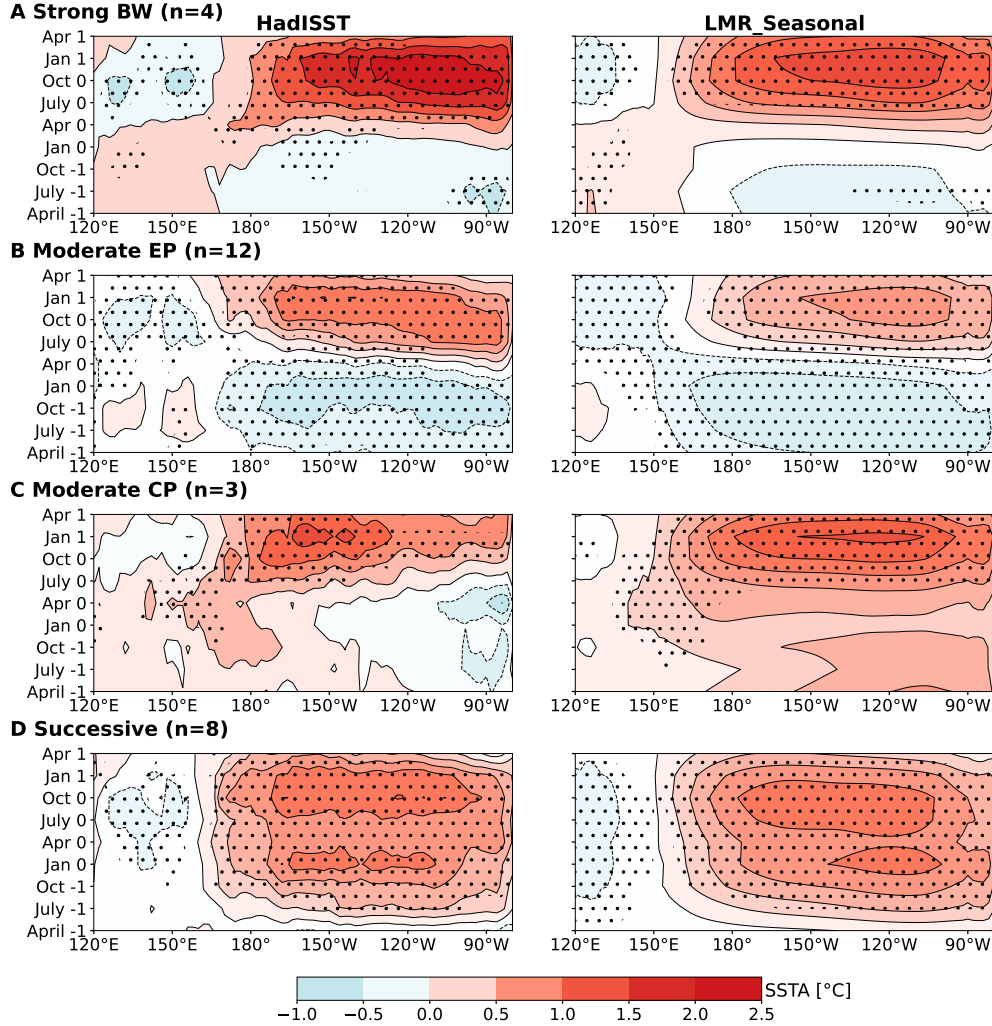


Figure 9: **Verification of the four classes of El Niño onset evolution of Wang et al. (2019) during 1900–2000.** The left column displays composite analyses from HadISST (Rayner et al., 2003), and the right column shows the LMR Seasonal Reconstruction. Rows show composite averages of the four El Niño classes: Strong Basin-Wide (SBW) (A), Moderate Eastern Pacific (MEP) (B), Moderate Central Pacific (MCP) (C), and Successive (D). Black dots show the composite SST anomaly values passing the confidence level of 95% using the Student T-test.

factors collectively contribute to the distinct differences we observe between the MCA and LIA. To test this hypothesis, we perform another experiment, allowing seasonal proxies to update only the annual mean during assimilation. Results show that the global-mean temperature difference between the MCA and LIA decreases by 30%, from 0.15°C to 0.10°C . In this case, our seasonal-update strategy appears to be essential to reconstructing the magnitude of the MCA-LIA difference.

Differences between the MCA and LIA are also evident in sea-ice area, sea-ice volume and OHC300 (Fig. 14). Specifically, sea-ice area increases around 5% from $1.1 \times 10^{13} \text{m}^2$ to $1.15 \times 10^{13} \text{m}^2$ from the MCA to the LIA. Sea-ice volume increases by about 11% from $3.5 \times 10^{13} \text{m}^3$ to $3.9 \times 10^{13} \text{m}^3$, which we attribute to the longer persistence time of sea-ice volume relative to area (Guemas et al., 2016). Compared to the sea-ice area reconstruction of Brennan and Hakim (2022), we find largely similar centennial-scale results (Fig. 14a). In particular, both reconstructions show a decline in sea-ice area that began in the early 19th century, and continues to the present. LMR Seasonal has less amplitude on decadal time scales, which is especially evident during the Early Twentieth Century Warming (1920–1950). We attribute this difference to weak co-variability between 2-m air temperature and sea-ice in the CCSM4 LM simulation, which Brennan and Hakim (2022) rectified with covariance inflation; here we do not use covariance inflation. Finally, we note that differences in OHC300 show a decrease from the MCA to LIA of about $1\text{--}1.5 \times 10^8 \text{J/m}^2$, or an average of

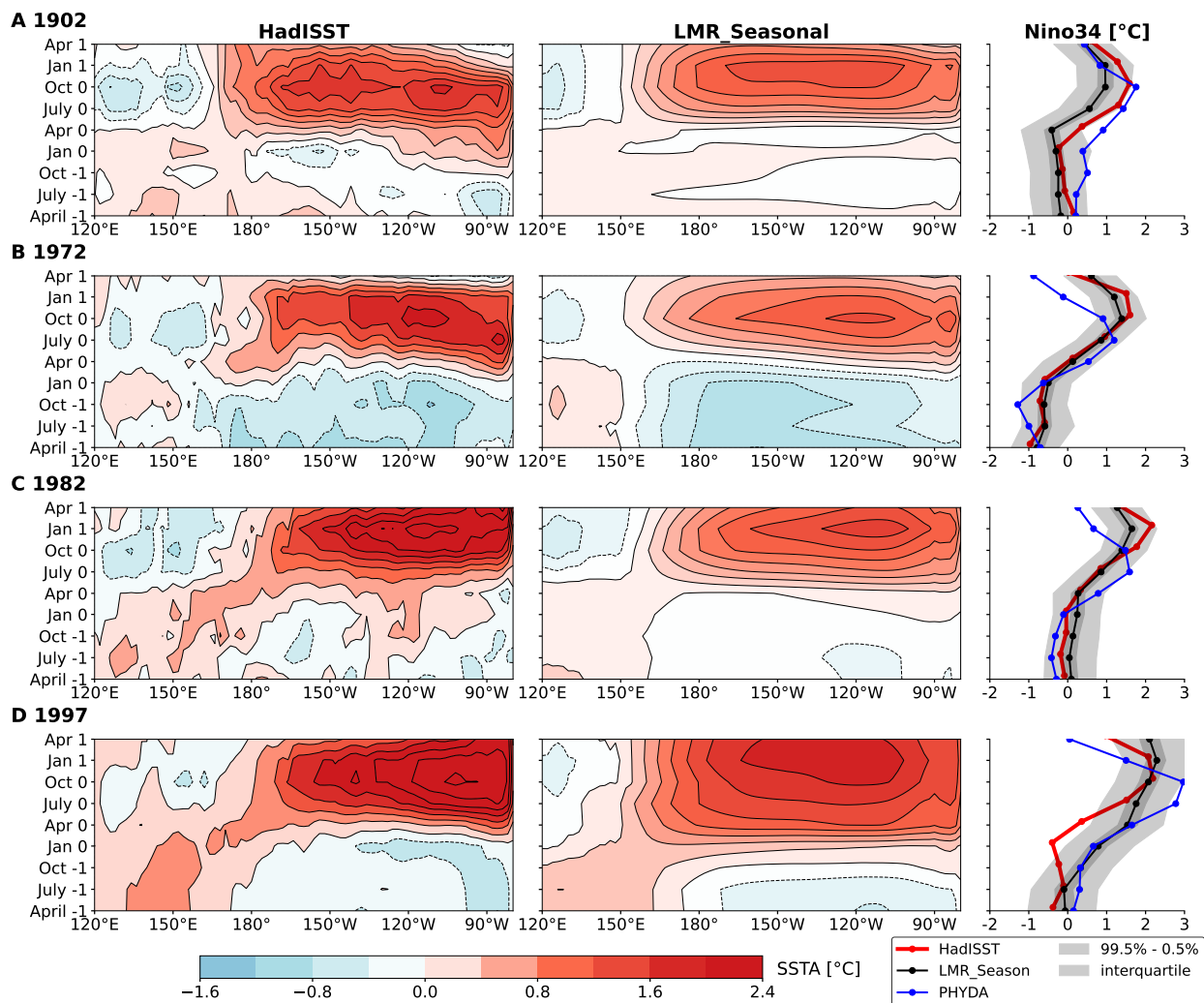


Figure 10: Verification of four Strong Basin-Wide (Super) El Niño Cases' onset evolution (1902, 1972, 1982, and 1997). The left column shows the evolution in HadISST (Rayner et al., 2003), and the middle column represents the LMR Seasonal Reconstruction. The right column depicts the time series of the Niño 3.4 Index from HadISST (red), PHYDA (blue) and LMR Seasonal reconstruction mean (black). The dark shading denotes the interquartile range, and light shading denotes the central 99% confidence interval.

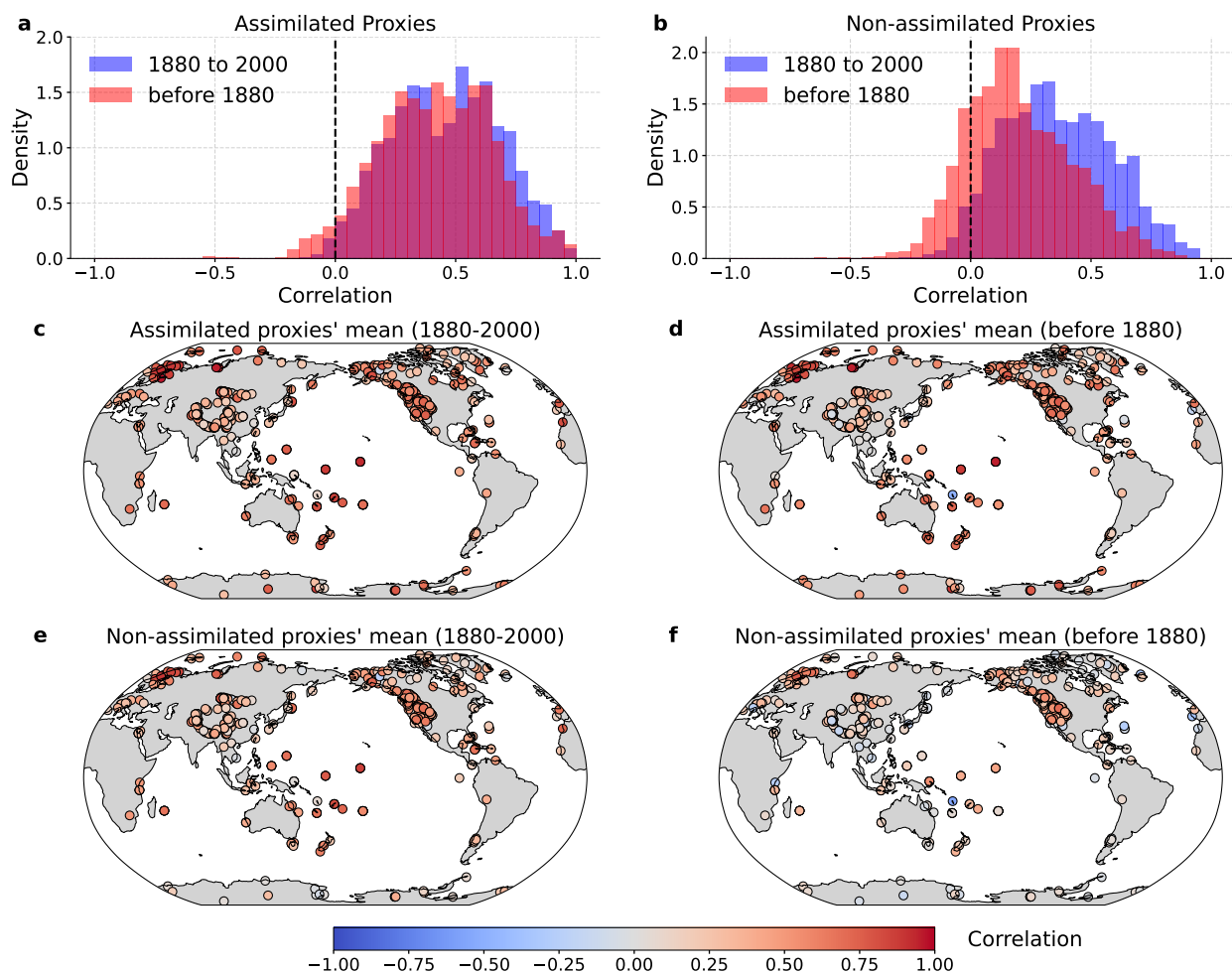


Figure 11: **Verification of LMR Seasonal against assimilated and non-assimilated proxy data.** The top row illustrates the distribution of correlation values between proxy values and LMR Seasonal estimates for assimilated (a) and non-assimilated (b) proxy data from 1880–2000 (blue) and prior to 1880 (red). The middle row shows proxy time-mean correlation maps for assimilated proxies during 1880–2000 (c) and before 1880 (d), and the bottom row for non-assimilated proxies during 1880–2000 (e) and before 1880 (f).

about 10 mW/m^2 . We note that the overall trend in ocean heat content is similar to that shown in [Gebbie and Huybers \(2019\)](#).

5 Discussion and Conclusions

This study introduces LMR Seasonal, a new reconstruction of coupled atmosphere–ocean–sea-ice climate variability over the Last Millennium, using a novel seasonal “online” data assimilation method and a new seasonal update strategy. The reconstruction is skillful in both space and time when compared with instrumental observations across the climate variables considered. Skill is primarily attributed to the efficient utilization of proxy information, allowing for updates to model forecasts during assimilation that accurately reflect seasonal variability in the proxies. Additionally, verification against independent (non-assimilated) proxies shows the robustness of the reconstruction in the pre-instrumental period.

We used the new reconstruction to examine two key measures of climate variability over the last millennium: ENSO and pre-instrumental trends related to the transition from the Medieval Climate Anomaly to the Little Ice Age. For ENSO, LMR Seasonal is able to accurately capture the space–time evolution of tropical SST for four different ENSO categories during the 20th century. Given the large increase in sample size of ENSO over the last millennium compared to the 20th and 21st centuries, LMR Seasonal potentially offers a new resource for ENSO research. For temperature trends of the last millennium, we find that LMR Seasonal captures seasonal variability consistent with orbital forcing, including

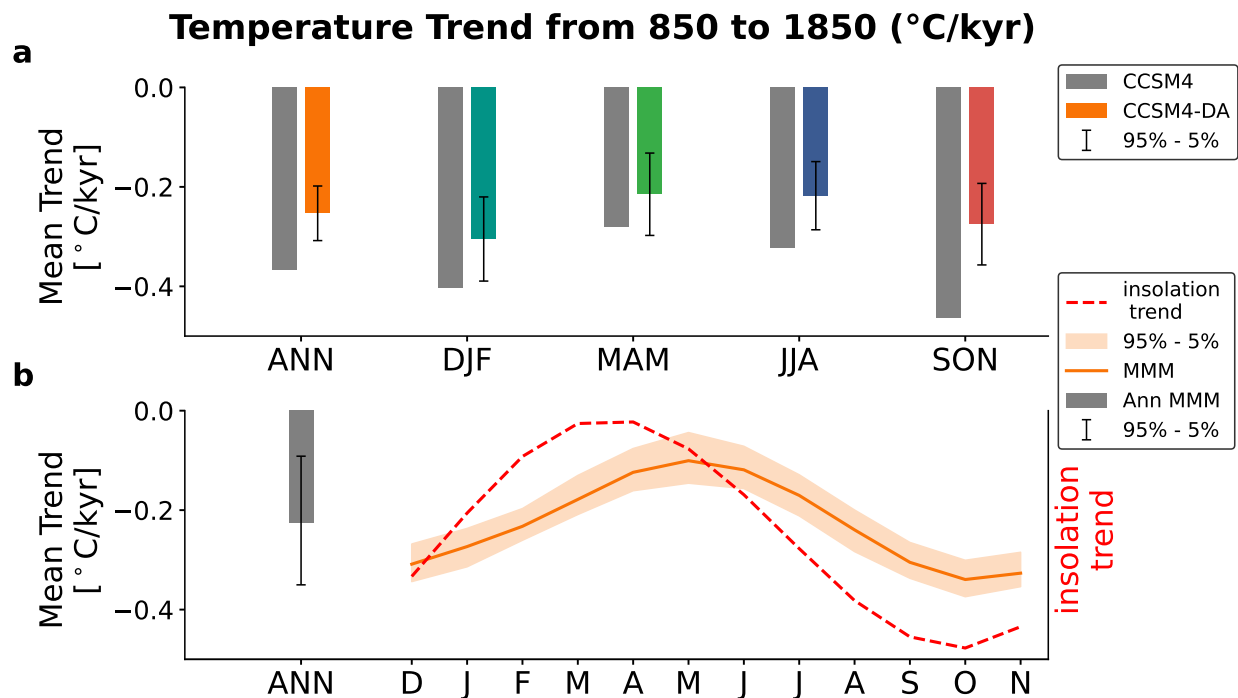


Figure 12: **Comparison of Last Millennium (LM) global-mean temperature trends for LMR Seasonal and the Climate Model LM simulations.** **a.** The global mean temperature trend for the annual mean and each season. The gray bar denotes the CCSM4 LM simulation, and the colors LMR Seasonal. Error bars indicate the 90% ensemble confidence interval. **b.** The global-mean temperature trends for the annual mean (gray bar) and each month (orange solid line) from the Last Millennium CMIP5 Multi-Model Large Ensemble (CCSM4, CESM-LME, CSIRO-Mk3L-1-2, MPI-ESM-P, IPSL-CM5A-LR and HadCM3) (Taylor et al., 2012). The top-of-atmosphere insolation trend (right y-axis) is shown in the red dashed line (Laskar et al., 2004). Error bars and orange shading represent the central 90% confidence interval.

polar amplification. Moreover, LMR Seasonal demonstrates a pronounced distinction between the Medieval Climate Anomaly (MCA) and the Little Ice Age (LIA), consistent with established climatological studies. This distinction is significantly enhanced by the seasonal updating scheme, which ensures that summer-biased proxies do not dilute the cooler signatures of other seasons during the LIA.

Future studies could expand upon this work by incorporating additional proxy data and exploring regional climate events during the Last Millennium with much larger samples than are available with instrumental reanalyses. Moreover, extending this approach to reconstructions at finer spatial resolution could provide deeper insights into regional climate phenomena and their global implications.

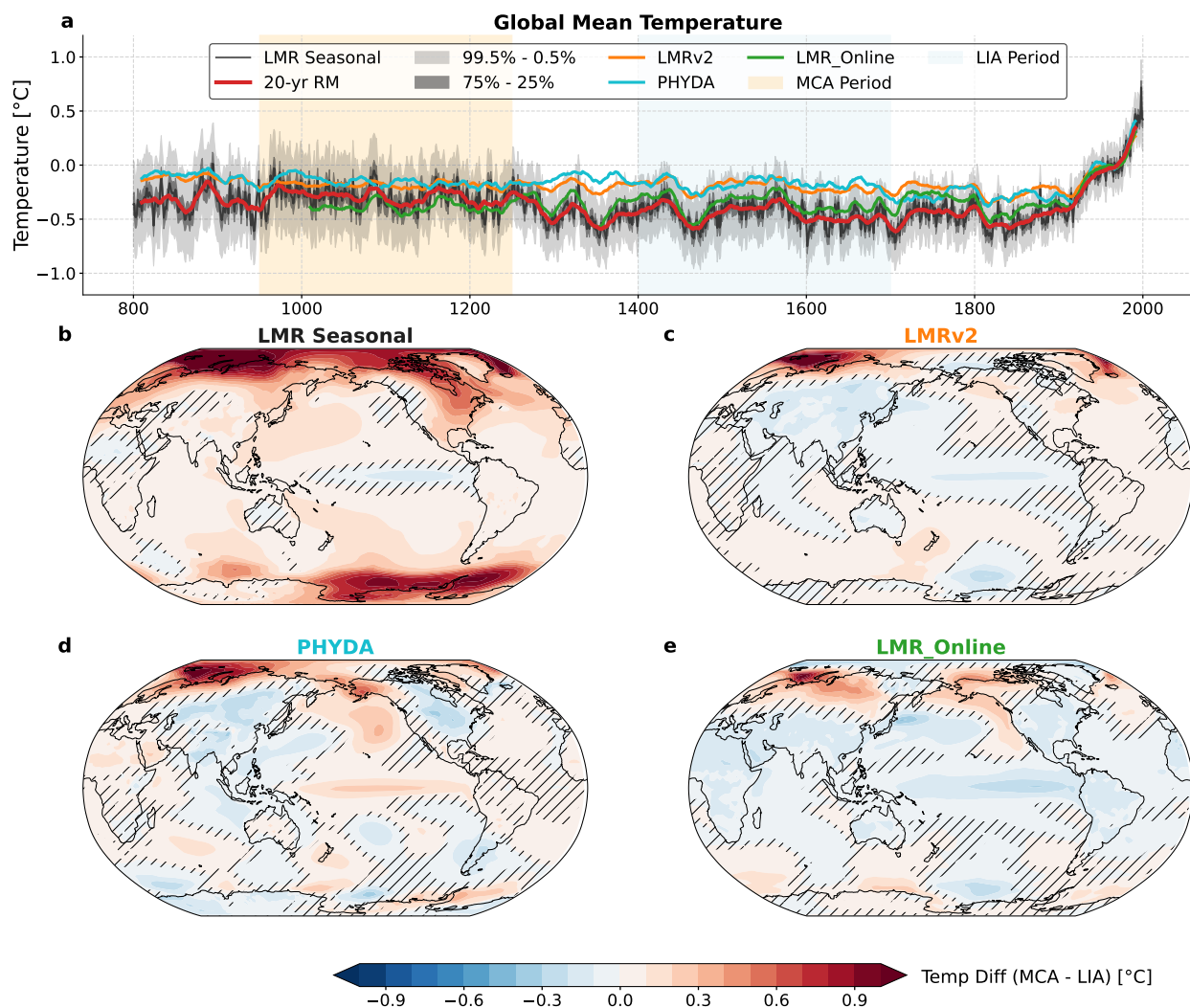


Figure 13: **Differences Between the Medieval Climate Anomaly (MCA, 950CE–1250CE) and Little Ice Age (LIA, 1400CE–1700CE) in four DA Reconstructions.** **a.** Global Mean Surface Temperature (GMT) 20-year running mean in LMR Seasonal (red), LMRv2 (yellow), LMR Online (green), and PHYDA (blue). The black solid curve represents the LMR Seasonal unsmoothed GMT, dark shading the interquartile range, and light shading the central 99% confidence interval. **b–e.** Global temperature pattern differences between MCA and LIA from LMR Seasonal (**b**), LMRv2 (**c**), PHYDA (**d**), and LMR Online (**e**). Hatching denotes regions that do not pass the 95% confidence level according to Student’s t-test.

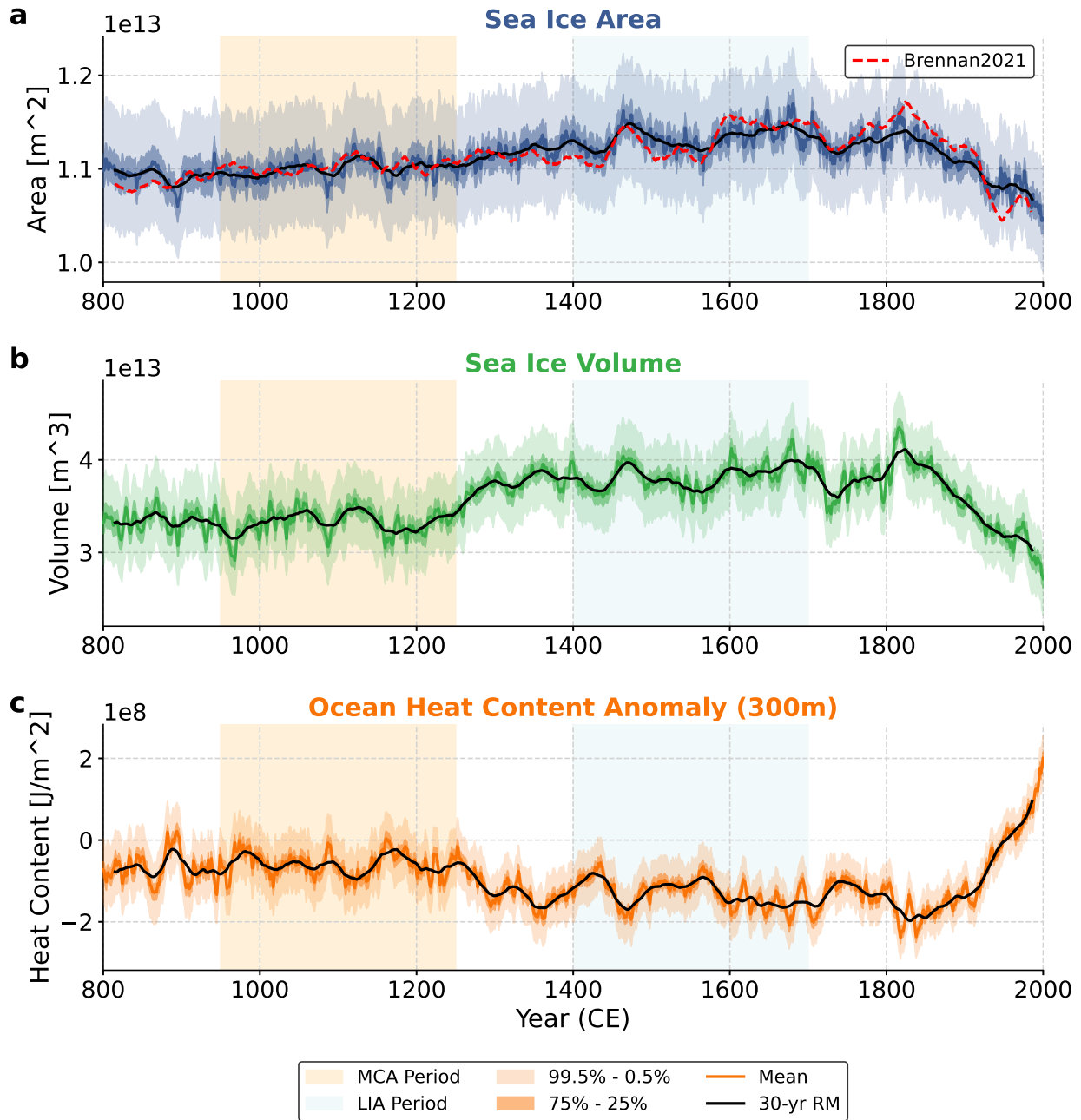


Figure 14: **Time series of Arctic sea-ice area (a) and volume (b), and upper 300m ocean heat content anomaly (c) over the last millennium.** The solid colored lines represent the ensemble mean, black solid lines denote the 30-year running means, dark shading the interquartile range, and light shading the central 99% confidence interval. The red dashed line in (a) is the 30-year running mean of sea-ice area from Brennan and Hakim (2022). Light orange shading denotes the MCA and light blue shading the LIA.

ACKNOWLEDGMENTS

This research was supported by NSF awards 2402475, 2202526 and 2105805, and Heising-Simons Foundation award 2023-4715. We appreciate comments and conversations related to this work with Feng Zhu (NSF National Center for Atmospheric Research), Olivia Truax (University of Canterbury), Julien Emile-Geay (University of Southern California), Dominik Stiller (University of Washington) and Vince Cooper (University of Washington).

DATA AVAILABILITY STATEMENT

The PSM package “CFR” (Zhu et al., 2023, 2024) and PAGES2K database are located at <https://github.com/fzhu2e/cfr>. The plotting package SACPYPY (Meng et al., 2021, 2023) is located at <https://github.com/ZiluM/sacpy>. The LMR Seasonal reconstruction data and code will be released to the public once this manuscript has been accepted.

References

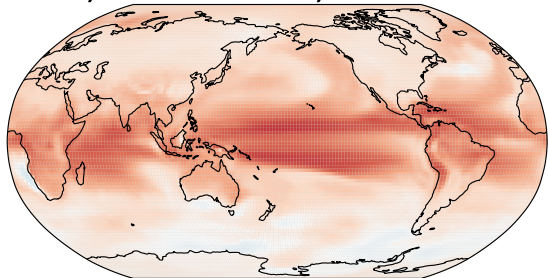
- Anchukaitis, K. J., and Coauthors, 2017: Last millennium Northern Hemisphere summer temperatures from tree rings: Part II, spatially resolved reconstructions. *Quaternary Science Reviews*, **163**, 1–22.
- Anderson, J. L., 2012: Localization and sampling error correction in ensemble Kalman filter data assimilation. *Monthly Weather Review*, **140** (7), 2359–2371.
- Blanchard-Wrigglesworth, E., K. C. Armour, C. M. Bitz, and E. DeWeaver, 2011: Persistence and inherent predictability of Arctic sea ice in a GCM ensemble and observations. *Journal of Climate*, **24** (1), 231–250.
- Bouttier, F., and P. Courtier, 2002: Data assimilation concepts and methods March 1999. *Meteorological training course lecture series. ECMWF*, **718**, 59.
- Brennan, M. K., 2022: *Reconstructing Arctic Sea Ice in the Instrumental Era*. University of Washington.
- Brennan, M. K., and G. J. Hakim, 2022: Reconstructing Arctic sea ice over the Common Era using data assimilation. *Journal of Climate*, **35** (4), 1231–1247.
- Briffa, K. R., P. D. Jones, and F. H. Schweingruber, 1992: Tree-ring density reconstructions of summer temperature patterns across western North America since 1600. *Journal of Climate*, **5** (7), 735–754.
- Briffa, K. R., T. J. Osborn, and F. H. Schweingruber, 2004: Large-scale temperature inferences from tree rings: a review. *Global and planetary change*, **40** (1-2), 11–26.
- Brown, J. R., and Coauthors, 2020: Comparison of past and future simulations of ENSO in CMIP5/PMIP3 and CMIP6/PMIP4 models. *Climate of the Past*, **16** (5), 1777–1805.
- Dee, S., Y. Okumura, S. Stevenson, and P. Di Nezio, 2020: Enhanced North American ENSO teleconnections during the Little Ice Age revealed by paleoclimate data assimilation. *Geophysical Research Letters*, **47** (15), e2020GL087504.
- Dirren, S., and G. J. Hakim, 2005: Toward the assimilation of time-averaged observations. *Geophysical research letters*, **32** (4).
- Evensen, G., 2003: The ensemble Kalman filter: Theoretical formulation and practical implementation. *Ocean dynamics*, **53**, 343–367.
- Fetterer, F., K. Knowles, W. Meier, M. Savoie, and A. Windnagel, 2017: Sea Ice Index, Version 3 [Data Set]. Boulder, Colorado USA. National Snow and Ice Data Center.
- Franke, J., S. Brönnimann, J. Bhend, and Y. Brugnara, 2017: A monthly global paleo-reanalysis of the atmosphere from 1600 to 2005 for studying past climatic variations. *Scientific data*, **4** (1), 1–19.
- Gebbie, G., and P. Huybers, 2019: The little ice age and 20th-century deep Pacific cooling. *Science*, **363** (6422), 70–74.
- Good, S. A., M. J. Martin, and N. A. Rayner, 2013: EN4: Quality controlled ocean temperature and salinity profiles and monthly objective analyses with uncertainty estimates. *Journal of Geophysical Research: Oceans*, **118** (12), 6704–6716.
- Goosse, H., E. Cresspin, A. de Montety, M. Mann, H. Renssen, and A. Timmermann, 2010: Reconstructing surface temperature changes over the past 600 years using climate model simulations with data assimilation. *Journal of Geophysical Research: Atmospheres*, **115** (D9).
- Guemas, V., and Coauthors, 2016: A review on Arctic sea-ice predictability and prediction on seasonal to decadal time-scales. *Quarterly Journal of the Royal Meteorological Society*, **142** (695), 546–561.
- Hakim, G. J., J. Emile-Geay, E. J. Steig, D. Noone, D. M. Anderson, R. Tardif, N. Steiger, and W. A. Perkins, 2016: The last millennium climate reanalysis project: Framework and first results. *Journal of Geophysical Research: Atmospheres*, **121** (12), 6745–6764.
- Hakim, G. J., C. Snyder, S. G. Penny, and M. Newman, 2022: Subseasonal forecast skill improvement from strongly coupled data assimilation with a linear inverse model. *Geophysical Research Letters*, **49** (11), e2022GL097996.
- Hu, W., and Coauthors, 2024: Reconstructing tropical monthly sea surface temperature variability by assimilating coral proxy datasets. *npj Climate and Atmospheric Science*, **7** (1), 261.
- Huang, B., and Coauthors, 2017: Extended reconstructed sea surface temperature, version 5 (ERSSTv5): upgrades, validations, and intercomparisons. *Journal of Climate*, **30** (20), 8179–8205.
- Laskar, J., P. Robutel, F. Joutel, M. Gastineau, A. C. Correia, and B. Levrard, 2004: A long-term numerical solution for the insolation quantities of the Earth. *Astronomy & Astrophysics*, **428** (1), 261–285.
- Lensen, N. J., G. A. Schmidt, J. E. Hansen, M. J. Menne, A. Persin, R. Ruedy, and D. Zyss, 2019: Improvements in the GISTEMP uncertainty model. *Journal of Geophysical Research: Atmospheres*, **124** (12), 6307–6326.

- Lücke, L. J., A. P. Schurer, R. Wilson, and G. C. Hegerl, 2021: Orbital forcing strongly influences seasonal temperature trends during the last millennium. *Geophysical Research Letters*, **48** (4), e2020GL088776.
- Luo, X., S. Dee, S. Stevenson, Y. Okumura, N. Steiger, and L. Parsons, 2022: Last millennium ENSO diversity and North American teleconnections: New insights from paleoclimate data assimilation. *Paleoceanography and Paleoclimatology*, **37** (3), e2021PA004283.
- Mann, M. E., and Coauthors, 2009: Global Signatures and Dynamical Origins of the Little Ice Age and Medieval Climate Anomaly. *Science*, **326** (5957), 1256–1260.
- Mantua, N. J., and S. R. Hare, 2002: The Pacific decadal oscillation. *Journal of oceanography*, **58**, 35–44.
- McGregor, H. V., and Coauthors, 2015: Robust global ocean cooling trend for the pre-industrial Common Era. *Nature Geoscience*, **8** (9), 671–677.
- McPhaden, M. J., S. E. Zebiak, and M. H. Glantz, 2006: ENSO as an integrating concept in earth science. *science*, **314** (5806), 1740–1745.
- Meng, Z., and G. J. Hakim, 2024: Reconstructing the tropical Pacific upper ocean using online data assimilation with a deep learning model. *Journal of Advances in Modeling Earth Systems*, **16** (11), e2024MS004422.
- Meng, Z., Z. Hu, Z. Ai, Y. Zhang, and K. Shan, 2021: Research on Planar Double Compound Pendulum Based on RK-8 Algorithm. *Journal on Big Data*, **3** (1), 11.
- Meng, Z., and T. Li, 2024: Why is the Pacific meridional mode most pronounced in boreal spring? *Climate Dynamics*, **62** (1), 459–471.
- Meng, Z., F. Zhu, and G. J. Hakim, 2023: Sacy–A Python Package for Statistical Analysis of Climate. *AGU23*.
- Morice, C. P., and Coauthors, 2021: An updated assessment of near-surface temperature change from 1850: The HadCRUT5 data set. *Journal of Geophysical Research: Atmospheres*, **126** (3), e2019JD032361.
- Nash, J. E., and J. V. Sutcliffe, 1970: River flow forecasting through conceptual models part I—A discussion of principles. *Journal of hydrology*, **10** (3), 282–290.
- Newman, M., 2013: An Empirical Benchmark for Decadal Forecasts of Global Surface Temperature Anomalies. *Journal of Climate*, **26** (14), 5260–5269, doi:10.1175/JCLI-D-12-00590.1.
- Okazaki, A., T. Miyoshi, K. Yoshimura, S. J. Greybush, and F. Zhang, 2021: Revisiting online and offline data assimilation comparison for paleoclimate reconstruction: An idealized OSSE study. *Journal of Geophysical Research: Atmospheres*, **126** (16), e2020JD034214.
- Orsi, A. J., B. D. Cornuelle, and J. P. Severinghaus, 2012: Little Ice Age cold interval in West Antarctica: evidence from borehole temperature at the West Antarctic Ice Sheet (WAIS) divide. *Geophysical Research Letters*, **39** (9).
- Pachauri, R. K., A. Reisinger, and Coauthors, 2007: IPCC fourth assessment report. *IPCC, Geneva*, **2007** (673), 044–023.
- PAGES2k Consortium, 2013: Continental-scale temperature variability during the past two millennia. *Nature geoscience*, **6** (5), 339–346.
- PAGES2k Consortium and others, 2017: A global multiproxy database for temperature reconstructions of the Common Era. *Scientific data*, **4**.
- Penland, C., and T. Magorian, 1993: Prediction of Niño 3 sea surface temperatures using linear inverse modeling. *Journal of Climate*, **6** (6), 1067–1076.
- Penland, C., and L. Matrosova, 1994: A balance condition for stochastic numerical models with application to the El Niño–Southern Oscillation. *Journal of climate*, **7** (9), 1352–1372.
- Penland, Cécile and Sardeshmukh, Prashant D, 1995: The optimal growth of tropical sea surface temperature anomalies. *Journal of climate*, **8** (8), 1999–2024.
- Perkins, W., and G. Hakim, 2021: Coupled atmosphere–ocean reconstruction of the last millennium using online data assimilation. *Paleoceanography and Paleoclimatology*, **36** (5), e2020PA003959.
- Perkins, W. A., and G. Hakim, 2020: Linear Inverse Modeling for Coupled Atmosphere–Ocean Ensemble Climate Prediction. *Journal of Advances in Modeling Earth Systems*, **12** (1), e2019MS001778.
- Poli, P., and Coauthors, 2016: ERA-20C: An atmospheric reanalysis of the twentieth century. *Journal of Climate*, **29** (11), 4083–4097.
- Rayner, N., D. E. Parker, E. Horton, C. K. Folland, L. V. Alexander, D. Rowell, E. C. Kent, and A. Kaplan, 2003: Global analyses of sea surface temperature, sea ice, and night marine air temperature since the late nineteenth century. *Journal of Geophysical Research: Atmospheres*, **108** (D14).

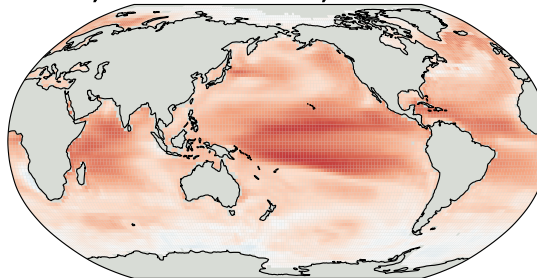
- Roach, L. A., and Coauthors, 2020: Antarctic sea ice area in CMIP6. *Geophysical Research Letters*, **47** (9), e2019GL086729.
- Rohde, R. A., and Z. Hausfather, 2020: The Berkeley Earth land/ocean temperature record. *Earth System Science Data*, **12** (4), 3469–3479.
- Schulzweida, U., L. Kornblueh, and R. Quast, 2019: CDO user guide.
- Smith, T. M., R. W. Reynolds, T. C. Peterson, and J. Lawrimore, 2008: Improvements to NOAA's historical merged land–ocean surface temperature analysis (1880–2006). *Journal of climate*, **21** (10), 2283–2296.
- Steig, E. J., and Coauthors, 2013: Recent climate and ice-sheet changes in West Antarctica compared with the past 2,000 years. *Nature Geoscience*, **6** (5), 372–375.
- Steiger, N. J., J. E. Smerdon, E. R. Cook, and B. I. Cook, 2018: A reconstruction of global hydroclimate and dynamical variables over the Common Era. *Scientific data*, **5** (1), 1–15.
- Steiger, N. J., E. J. Steig, S. G. Dee, G. H. Roe, and G. J. Hakim, 2017: Climate reconstruction using data assimilation of water isotope ratios from ice cores. *Journal of Geophysical Research: Atmospheres*, **122** (3), 1545–1568, doi:<https://doi.org/10.1002/2016JD026011>.
- Stenni, B., and Coauthors, 2017: Antarctic climate variability on regional and continental scales over the last 2000 years. *Climate of the Past*, **13** (11), 1609–1634, doi:[10.5194/cp-13-1609-2017](https://doi.org/10.5194/cp-13-1609-2017).
- Sun, H., L. Lei, Z. Liu, L. Ning, and Z.-M. Tan, 2022: An analog offline EnKF for paleoclimate data assimilation. *Journal of Advances in Modeling Earth Systems*, **14** (5), e2021MS002674.
- Tardif, R., and Coauthors, 2019: Last Millennium Reanalysis with an expanded proxy database and seasonal proxy modeling. *Climate of the Past*, **15** (4), 1251–1273.
- Taylor, K. E., R. J. Stouffer, and G. A. Meehl, 2012: An overview of CMIP5 and the experiment design. *Bulletin of the American meteorological Society*, **93** (4), 485–498.
- Valler, V., and Coauthors, 2024: ModE-RA: a global monthly paleo-reanalysis of the modern era 1421 to 2008. *Scientific data*, **11** (1), 36.
- Wang, B., X. Luo, Y.-M. Yang, W. Sun, M. A. Cane, W. Cai, S.-W. Yeh, and J. Liu, 2019: Historical change of El Niño properties sheds light on future changes of extreme El Niño. *Proceedings of the National Academy of Sciences*, **116** (45), 22512–22517.
- Whitaker, J. S., and T. M. Hamill, 2002: Ensemble data assimilation without perturbed observations. *Monthly weather review*, **130** (7), 1913–1924.
- Widmann, M., H. Goosse, G. van der Schrier, R. Schnur, and J. Barkmeijer, 2010: Using data assimilation to study extratropical Northern Hemisphere climate over the last millennium. *Climate of the Past*, **6** (5), 627–644.
- Zhu, F., J. Emile-Geay, K. J. Anchukaitis, G. J. Hakim, A. T. Wittenberg, M. S. Morales, M. Toohey, and J. King, 2022: A re-appraisal of the ENSO response to volcanism with paleoclimate data assimilation. *Nature communications*, **13** (1), 747.
- Zhu, F., J. Emile-Geay, K. J. Anchukaitis, N. P. McKay, S. Stevenson, and Z. Meng, 2023: A pseudoproxy emulation of the PAGES 2k database using a hierarchy of proxy system models. *Scientific Data*, **10** (1), 624.
- Zhu, F., J. Emile-Geay, G. J. Hakim, D. Guillot, D. Khider, R. Tardif, and W. A. Perkins, 2024: cfr (v2024. 1.26): a Python package for climate field reconstruction. *Geoscientific Model Development*, **17** (8), 3409–3431.

Supporting Information (SI)

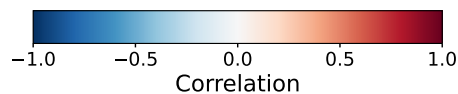
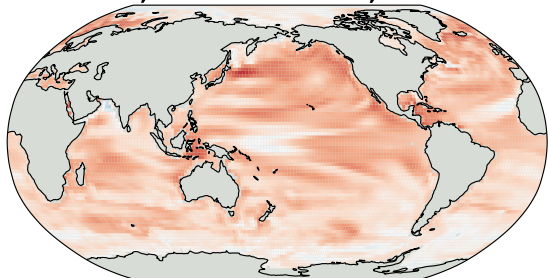
a. TAS; lead = 12 month; corr = 0.23



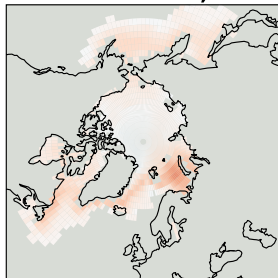
b. TOS; lead = 12 month; corr = 0.24



c. OHC300; lead = 12 month; corr = 0.22



d. SIC; lead = 12 month; corr = 0.06



e. SIT; lead = 12 month; corr = 0.39

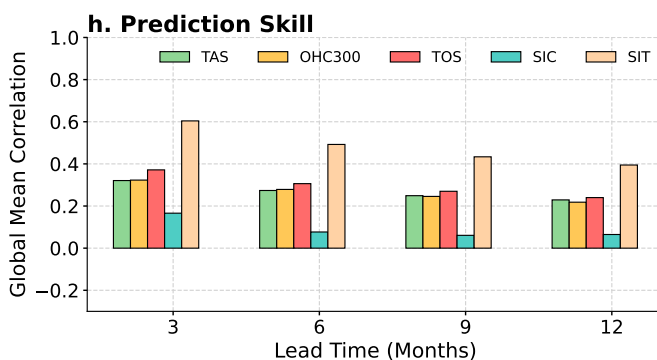
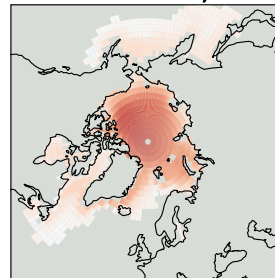
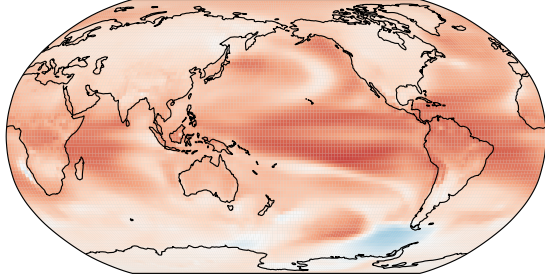
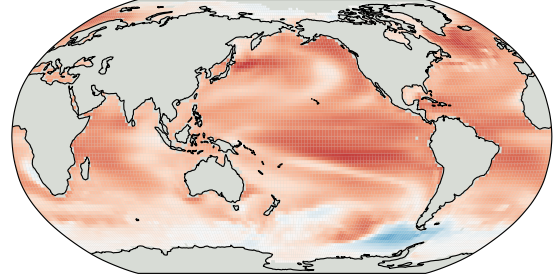


Figure S1: Forecast skill of the Linear Inverse Model (LIM) trained on CCSM4 tested on MPI-ESM-R. a-e. LIM correlation skill out-of-sample test on MPI-ESM-R at 12-month lead on TAS (a), TOS (b), OHC300 (c), SIC(d) and SIT (e). h. The global-mean forecast skill of different variables at lead time from 3 months to 12 months.

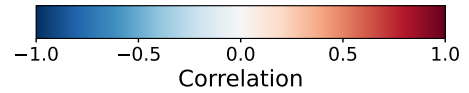
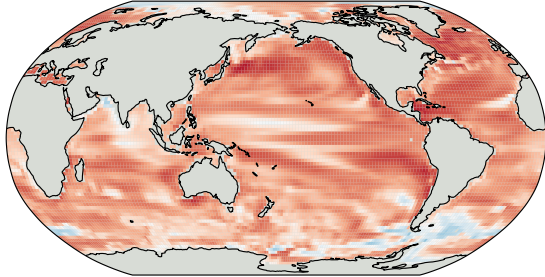
a. TAS; lead = 12 month; corr = 0.26



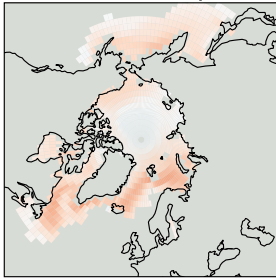
b. TOS; lead = 12 month; corr = 0.27



c. OHC300; lead = 12 month; corr = 0.35



d. SIC; lead = 12 month; corr = 0.08



e. SIT; lead = 12 month; corr = 0.43

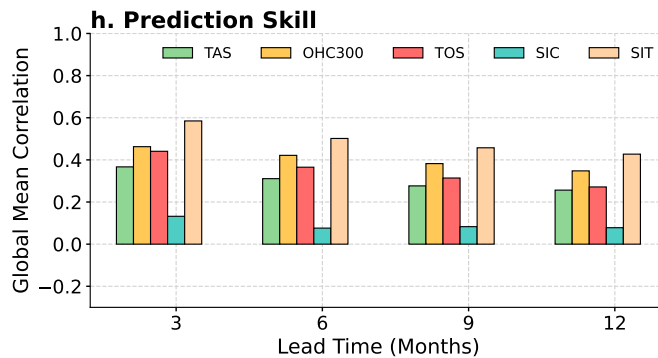
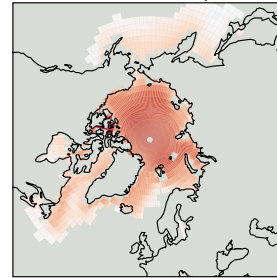


Figure S2: As in Figure S1, but for the LIM trained on MPI-ESM-R and tested on CCSM4.

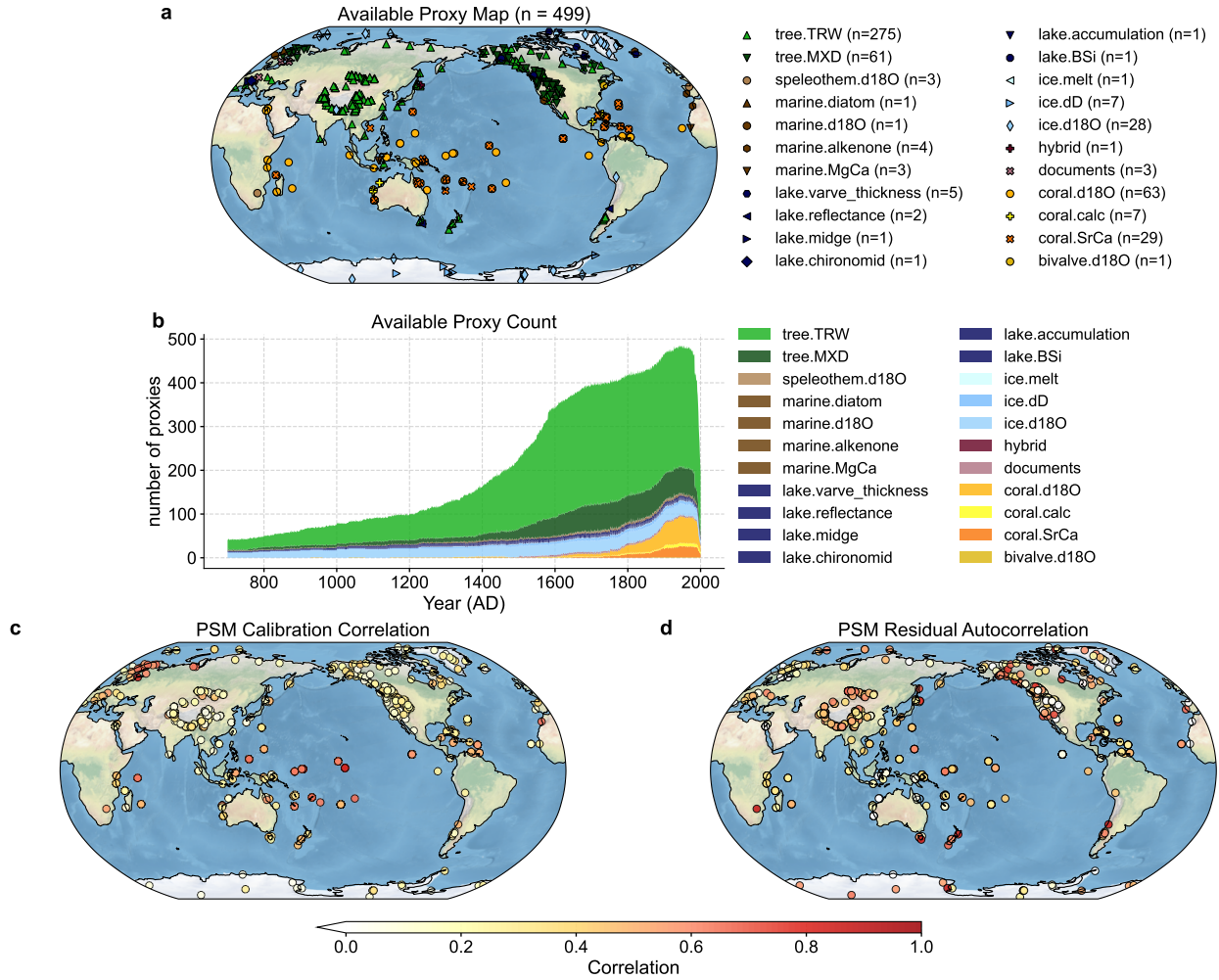
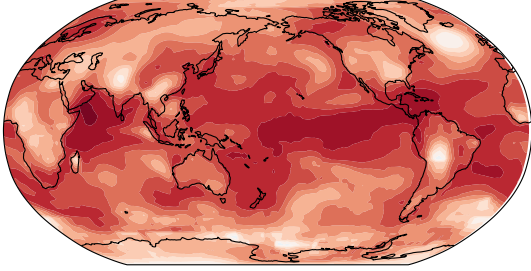
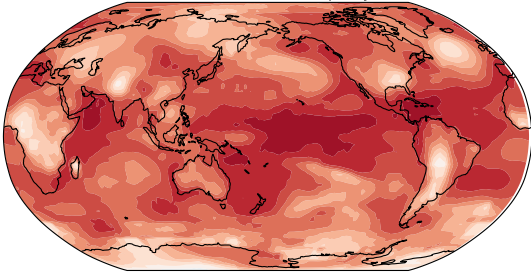


Figure S3: As in Figure 1, but for the expert-seasonality based PSM.

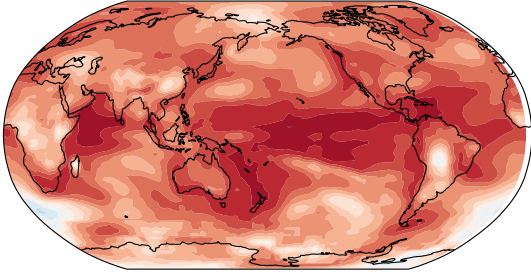
a LMR Seasonal (mean = 0.54, $N_{proxy} = 497$)



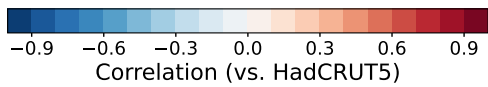
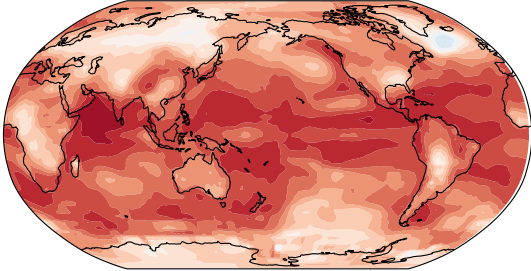
b LMRv2 (mean = 0.53, $N_{proxy} = 2250$)



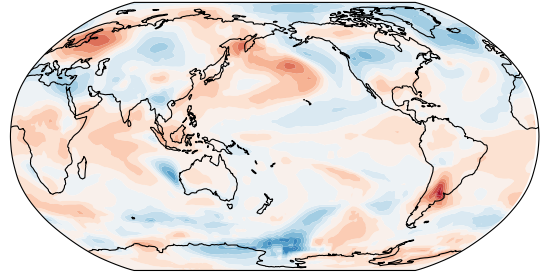
c PHYDA (mean = 0.50, $N_{proxy} = 2978$)



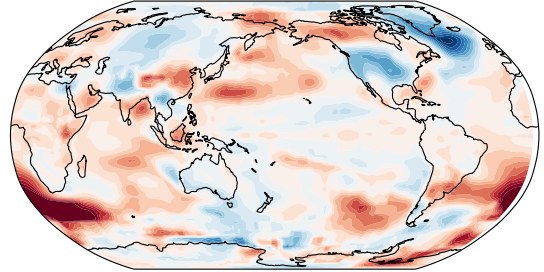
d LMR Online (mean = 0.47, $N_{proxy} = 545$)



f LMR Seasonal - LMRv2 (mean = 0.01)



g LMR Seasonal - PHYDA (mean = 0.04)



h LMR Seasonal - LMR Online (mean = 0.07)

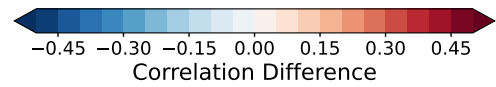
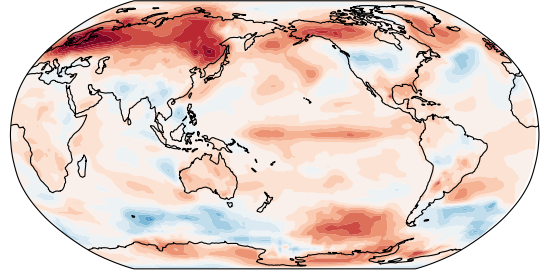


Figure S4: As in Figure 3, but for the expert-seasonality based PSM.

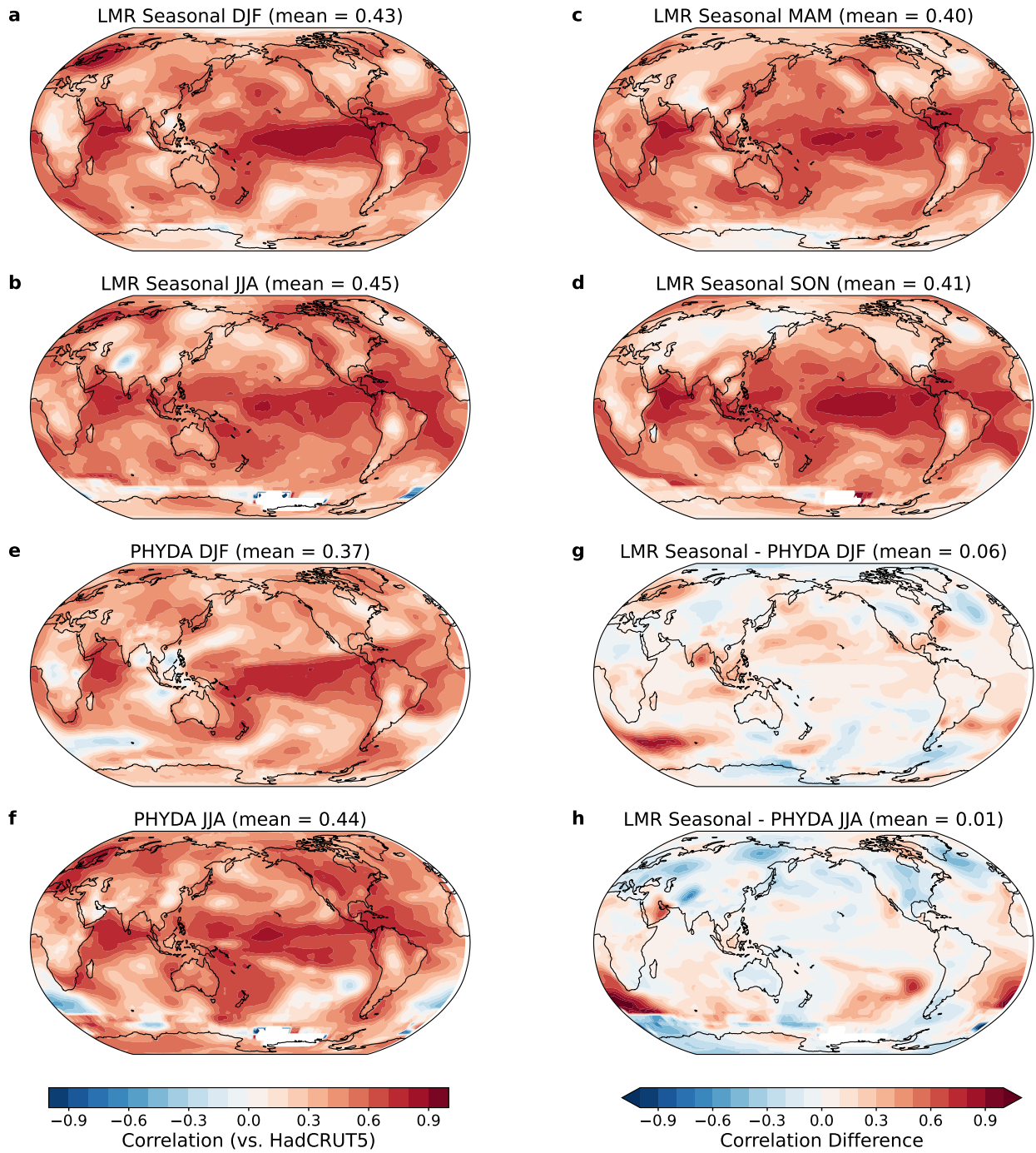


Figure S5: As in Figure 4, but for the expert-seasonality based PSM.

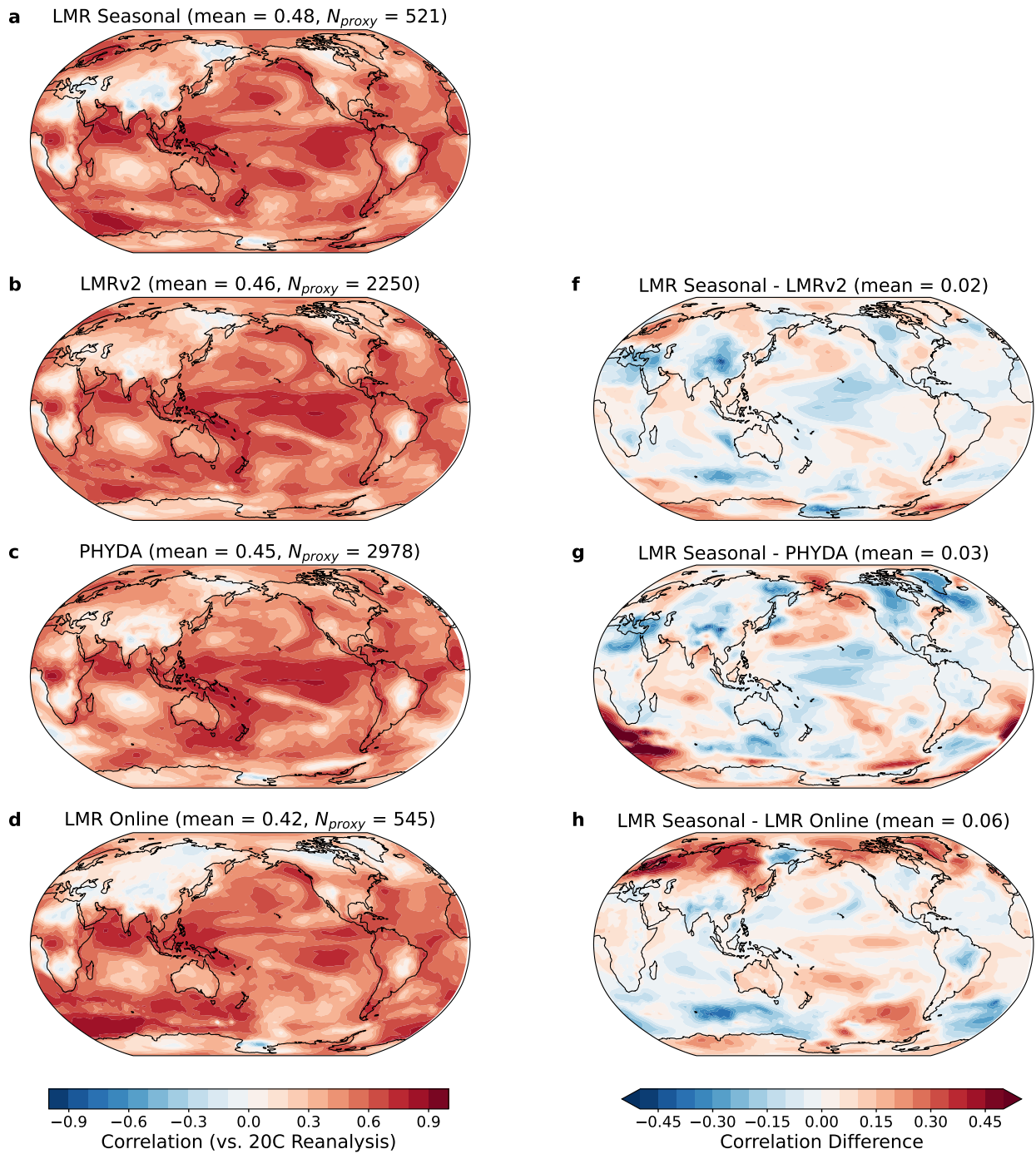


Figure S6: As in Figure 3, but for the correlation between reconstructions and ERA-20C Reanalysis.

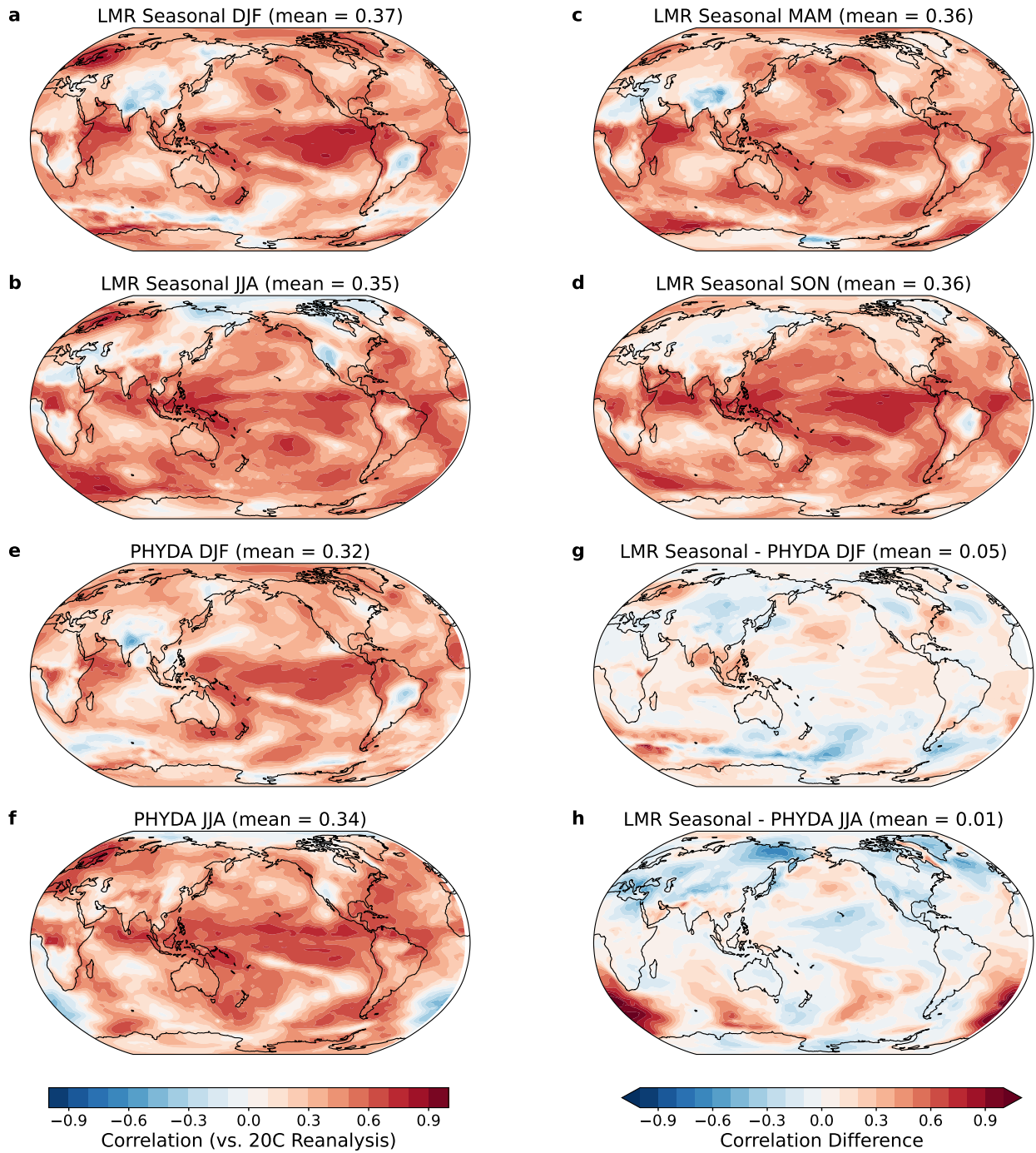


Figure S7: As in Figure 4, but for the correlation between reconstructions and ERA-20C Reanalysis.

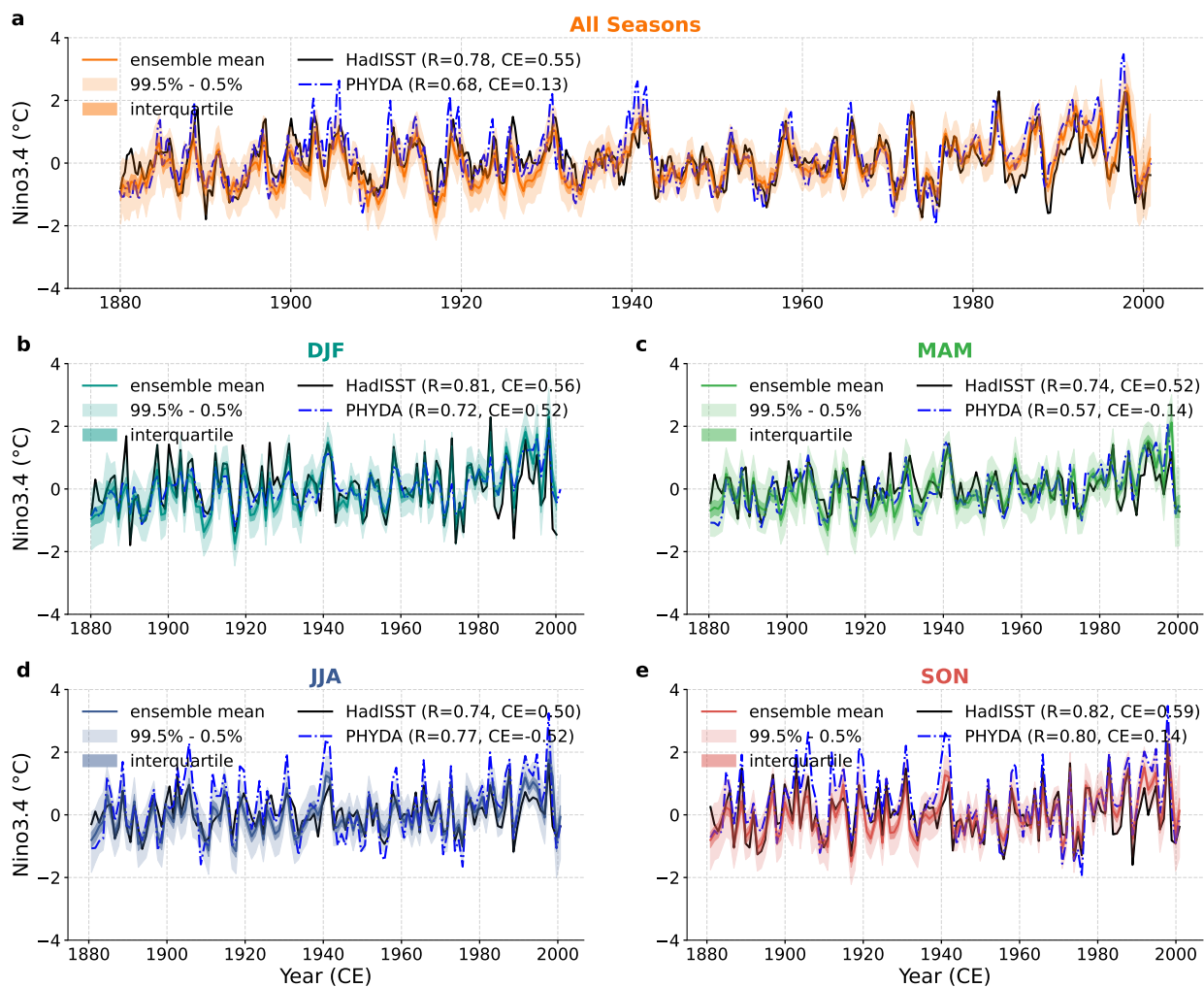


Figure S8: Same as Figure 8, but with the addition of the PHYDA-reconstructed Niño3.4 Index for comparison. The “R” and “CE” following HadISST (PHYDA) refer to the results comparing HadISST with LMR Seasonal (HadISST with PHYDA).

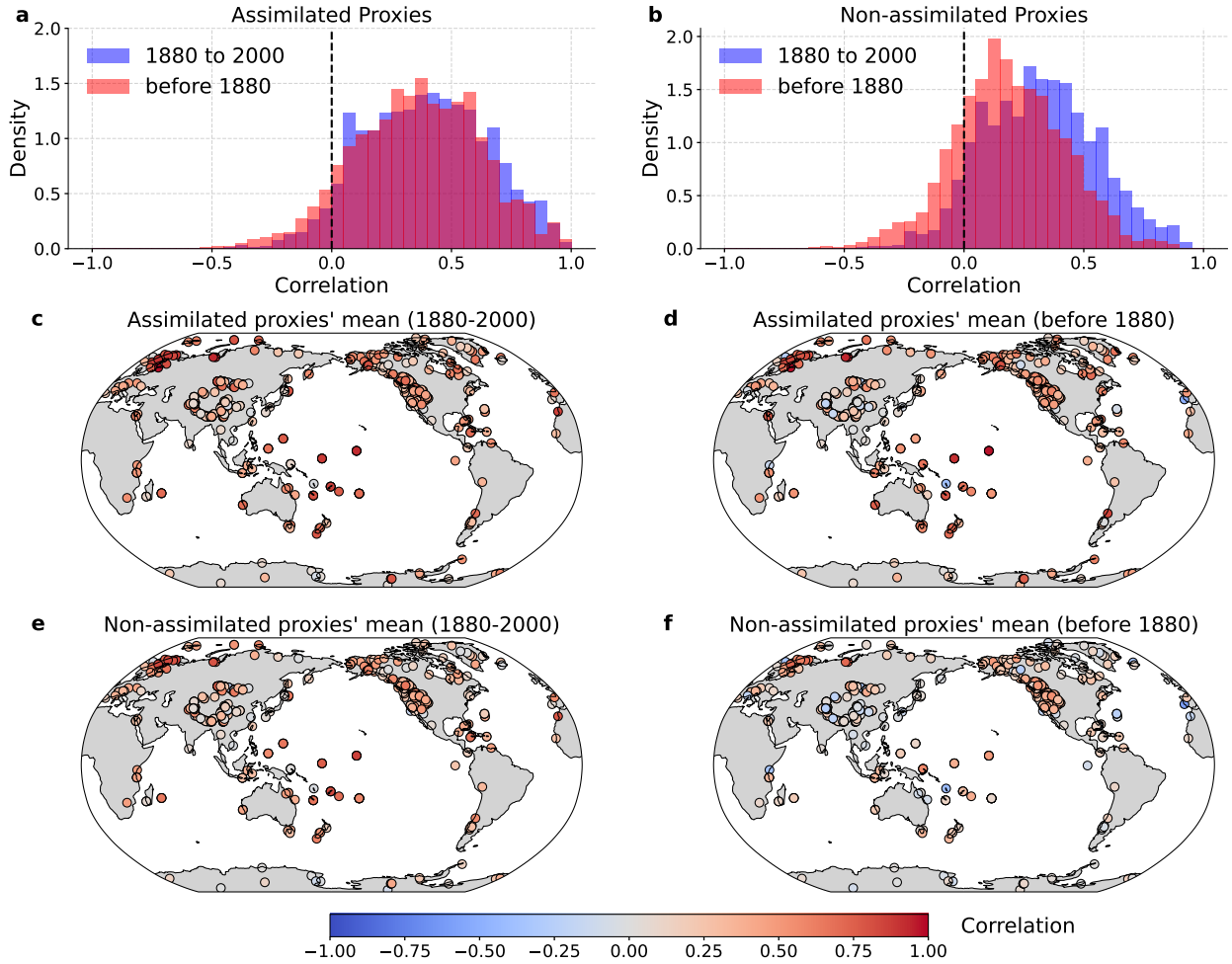


Figure S9: Same as Figure 11, but for the expert-seasonality based PSM.

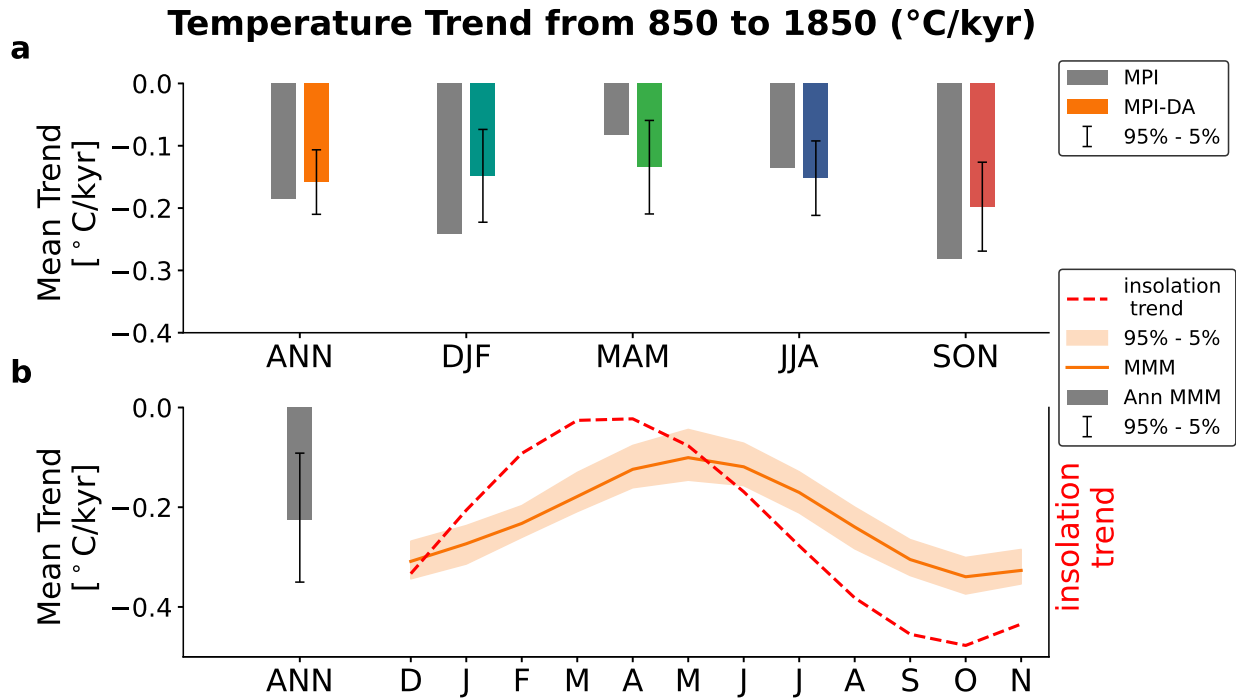


Figure S10: Same as Figure 12, but for the MPI-ESM-R based DA results and last millennium simulations.

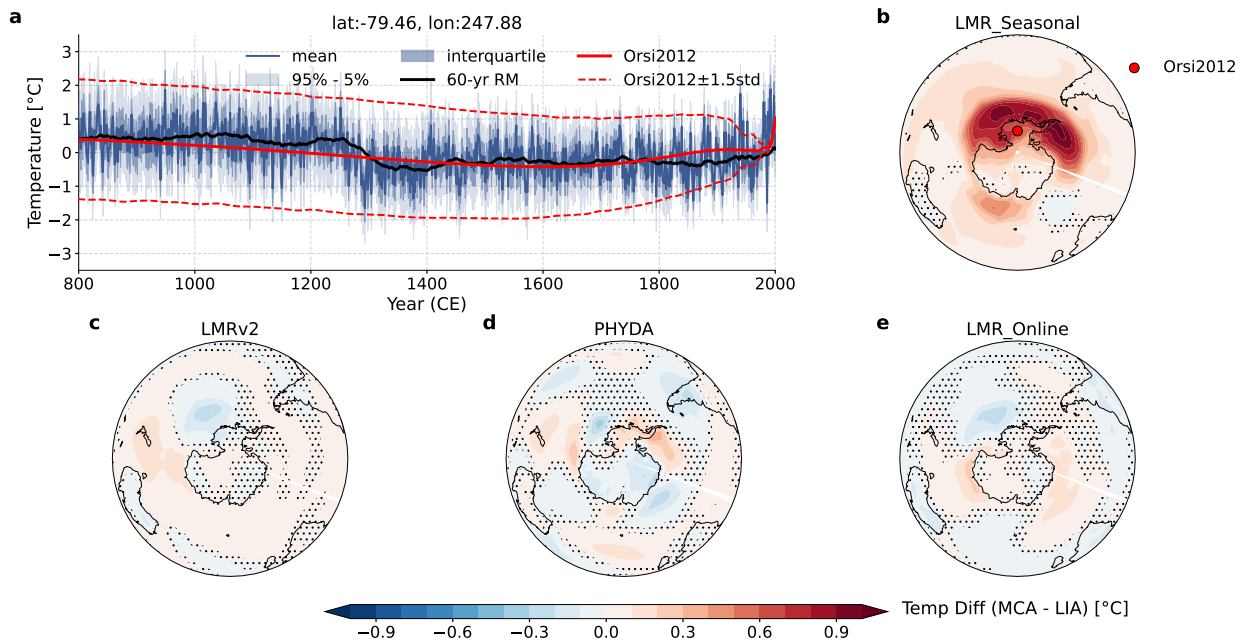


Figure S11: **Time Series of Temperature in West Antarctica (Latitude: -79.46° , Longitude: 247.88°) and MCA-LIA Temperature Difference Patterns in four PDA products.** (a) The solid blue colored lines represent the ensemble mean, black solid lines denote the 60-year running means, blue dark shading the interquartile ranges, and light shading the central 95% confidence intervals. The solid red line denotes the temperature reconstruction from the borehole in Orsi et al. (2012), while the dashed red line indicates the 1.5 standard deviation error bar of the borehole reconstruction. **b–e.** Southern Hemisphere temperature pattern differences between MCA and LIA from LMR Seasonal (b), LMRv2 (c), PHYDA (d), and LMR Online (e). Black dots denotes regions that do not pass the 95% confidence level according to Student's t-test. The red dot in (b) marks the location of the borehole.

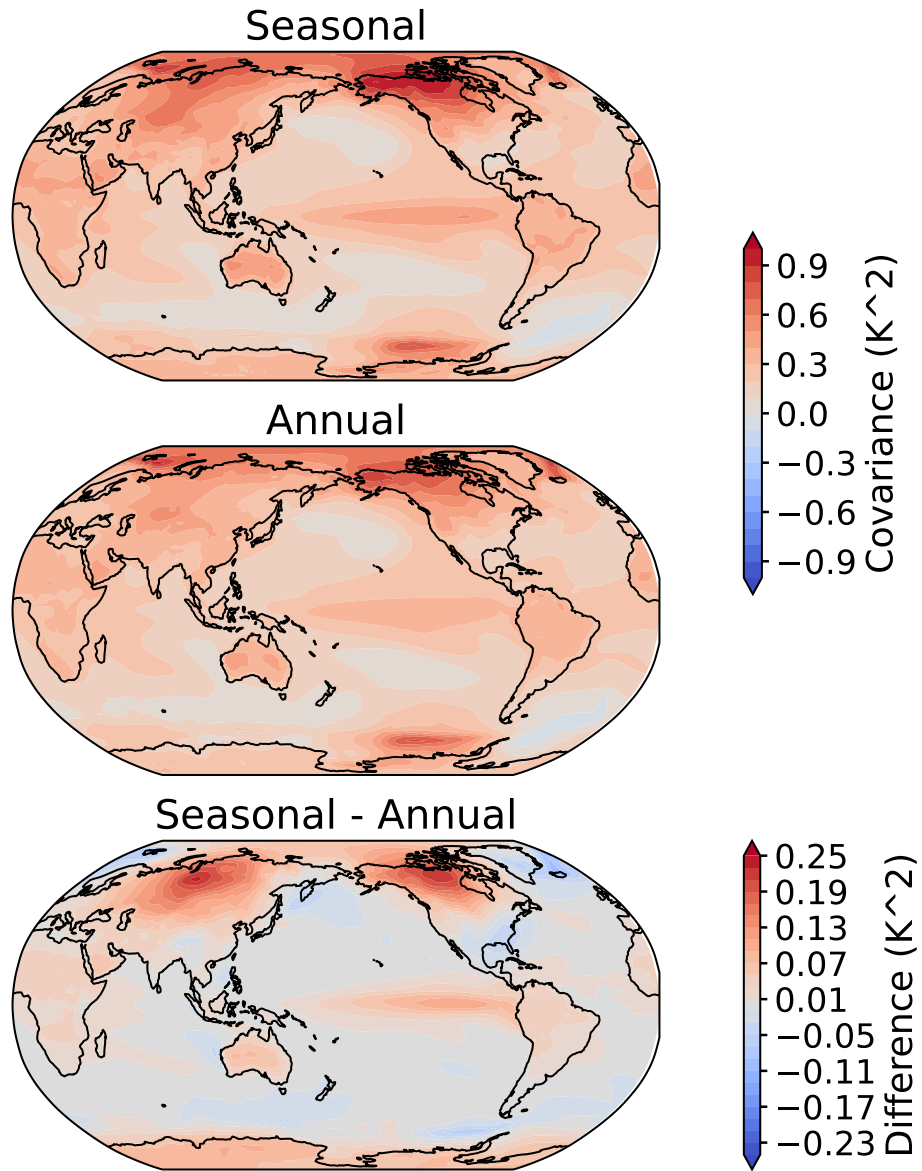


Figure S12: The covariance between global Mean Temperature and local temperature in seasonal time resolution (upper) and annual time resolution (middle) and their difference (lower) in the CCSM4 last millennium simulation.